Geomorphological map of the South Belet Region of Titan

Ashley M. Schoenfeld, Rosaly M.C. Lopes, Michael J. Malaska, Anezina Solomonidou, David A. Williams, Samuel P.D. Birch, Alexander G. Hayes, Paul Corlies, Alice Le Gall, Michael A. Janssen, et al.

Icarus 366 (2021) 114516

Contents lists available at ScienceDirect

Icarus

journal homepage: www.elsevier.com/locate/icarus

Research Paper

Geomorphological map of the South Belet Region of Titan

Ashley M. Schoenfeld [a,*], Rosaly M.C. Lopes [b], Michael J. Malaska [b], Anezina Solomonidou [c,d], David A. Williams [e], Samuel P.D. Birch [f], Alexander G. Hayes [g], Paul Corlies [f], Alice Le Gall [h,i], Michael A. Janssen [b], Stéphane Le Mouélic [j], Elizabeth Turtle [k], Meghan Florence [b], Tiffany Verlander [l]

[a] Department of Earth, Planetary, and Space Sciences, University of California, Los Angeles, Los Angeles, CA, USA
[b] Jet Propulsion Laboratory/California Institute of Technology, Pasadena, CA, USA
[c] California Institute of Technology, Pasadena, CA, USA
[d] Faculty of Environmental Sciences, Czech University of Life Sciences Prague, Suchdol, 16500 Praha, Czech Republic
[e] School of Earth and Space Exploration, Arizona State University, Tempe, AZ, USA
[f] Department of Earth, Atmospheric, and Planetary Science, Massachusetts Institute of Technology, Cambridge, MA, USA
[g] Department of Astronomy, Cornell University, Ithaca, NY, USA
[h] UVSQ CNRS Paris VI, UMR 8190, Atmospheres Lab, Observat Spatiales LATMOS, F-78280 Guyancourt, France
[i] Institut Universitaire de France, France
[j] LPG, UMR 6112, CNRS, Université de Nantes, 2 rue de la Houssinière, Nantes, France
[k] Johns Hopkins Applied Physics Laboratory, Laurel, MD, USA
[l] University of Oklahoma, School of Civil Engineering and Environmental Science, Norman, OK, USA

ARTICLE INFO

Keywords:
Titan
Geologic processes
Titan surface

ABSTRACT

We mapped in detail Titan's South Belet region which spans from longitude 60°E to 120°E and from latitude 60°S to 0°, encompassing both equatorial and southern mid-latitude regions. We used Cassini RADAR in its Synthetic Aperture Radar (SAR) mode data as our basemap, which covers 31.8% of the region, supplemented with data from the RADAR's radiometry mode, the Imagining Science Subsystem (ISS), the Visual and Infrared Mapping Spectrometer (VIMS), and topographic data. This mapping work is a continuation of the detailed global mapping effort introduced in Malaska et al. (2016a) and continued in Lopes et al. (2020). We followed the mapping procedure described in Malaska et al. (2016a) for the Afekan Crater region and identified four major terrain classes in South Belet: craters, hummocky/mountainous, plains, and dunes. Each terrain class was subdivided into terrain units by characteristic morphology, including border shape, texture, general appearance, and radar backscatter. There are two terrain units that were not included in previous studies but were identified in our mapping of South Belet: "bright alluvial plains" and "pitted hummocky". Similar to the Afekan Crater region, we find that plains dominate the surface make-up of South Belet, comprising ~47% of the mapped area. Unlike Afekan, the areal extent of the dunes closely rivals the dominance of plains, making up 43% of the mapped area. The next most widespread unit by area in the region following the dunes are the mountains/hummocky terrains (10%), and finally, crater terrains (0.01%). The introduction of two new units, "bright alluvial plains" and "pitted hummocky", are necessary to capture the full range of morphologies seen in South Belet and expands our understanding of processes typical of Titan's equatorial and mid-latitude regions. For example, the presence of alluvial fans indicates a period in Titan's past where discharges and slopes were such that sediment could be mobilized and deposited. Similarly, the pits associated with the "pitted hummocky" may represent an important erosional feature, with implications for the removal of volatiles from Titan's crust. However, analysis of our geomorphological mapping results suggests the geology of South Belet is consistent with the narrative of organics dominating the equatorial and mid-latitudes. This is similar to the conclusion we arrived at through our mapping and analysis of the Afekan region. Lastly, the applicability of the terrain units from our mapping of the Afekan region, which bears a similar latitude but in the northern hemisphere, to our mapping of South Belet suggests latitudinal symmetry in Titan's surface processes and their evolution.

* Corresponding author at: Department of Earth, Planetary, and Space Sciences, University of California, Los Angeles, 595 Charles Young Drive East, Box 951567, Los Angeles, CA 90095, USA.
E-mail address: ashley.schoenfeld@ucla.edu (A.M. Schoenfeld).

https://doi.org/10.1016/j.icarus.2021.114516
Received 2 November 2020; Received in revised form 20 April 2021; Accepted 29 April 2021
Available online 3 May 2021

1. Introduction

Saturn's largest moon Titan is the only natural satellite known to have a substantial atmosphere, a dense veil of nitrogen and methane obscuring the surface below. It was not until the Cassini-Huygens mission arrived in 2004 that Titan was revealed to be a geologically complex world, one characterized by mountains (Radebaugh et al., 2007; Cook-Hallett et al., 2015; Liu et al., 2016a, 2016b), dune fields (Lorenz et al., 2006; Radebaugh et al., 2008), lakes and seas (Stofan et al., 2007; Mitri et al., 2007; Brown et al., 2008; Hayes et al., 2008), channels (Perron et al., 2006; Lorenz et al., 2008; Burr et al., 2013a), putative cryovolcanism (Lopes et al., 2007, 2013; Le Corre et al., 2009; Mitri et al., 2019; Wood and Radebaugh, 2020), and other strikingly terrestrial-like features. Evidence for impact processes have also been identified, but their relative scarcity attest to a geologically young surface (Lorenz et al., 2007; Wood et al., 2010; Neish and Lorenz, 2012; Neish et al., 2013; Hedgepeth et al., 2020).

These familiar landforms inspire comparisons between terrestrial surface processes and processes currently or previously operating on Titan. A departure is found when considering their vastly different formation conditions. For example, Titan's surface is blanketed in organic materials, the result of long-term photochemical processing of methane and nitrogen in the upper atmosphere (e.g. Wilson and Atreya, 2004; Lavvas et al., 2008; Krasnopolsky, 2009, 2014). Titan's thick, nitrogen-dominated atmosphere allows for aeolian processes to shape the surface by transporting photochemically derived organic debris analogously to how silica or gypsum grains are transported on Earth (e.g. Barnes et al., 2015). Titan's equatorial zones are dominated by massive organic sand seas, whereas the mid-latitudes are dominated by "undifferentiated plains", a terrain interpreted as either vast aeolian deposits (Lopes et al., 2016) or vast lag deposits (Birch et al., 2016).

Titan also exhibits an active hydrological cycle, one where the precipitating fluid is methane and dissolved nitrogen, as opposed to water (Lorenz, 1993, 2000; Atreya et al., 2006; Hayes et al., 2018). Titan's surface temperature and pressure conditions are such that liquid methane is stable on the surface, and many observations suggest that liquid hydrocarbons have flowed energetically across Titan's surface, carving a variety of channel networks and fluvial valleys (Burr et al., 2009, 2013a, 2013b; Langhans et al., 2012; Birch et al., 2016; Radebaugh et al., 2018). Images taken from the Huygens probe, as it descended through Titan's atmosphere and after it landed, confirmed that liquids have modified the moon's surface, revealing a dense network of branching channels reminiscent of terrestrial river networks (Perron et al., 2006; Jaumann et al., 2008; Lunine and Lorenz, 2009; Langhans et al., 2012; Burr et al., 2013b). Numerous lakes and vast seas of liquid hydrocarbons are also found at high latitudes (Stofan et al., 2007; Mitri et al., 2007; Hayes et al., 2008; Birch et al., 2017).

In this paper, we describe our mapping of Titan's South Belet region and associated geomorphological terrain units. This region spans longitude 60°E to 120°E and from latitude 60°S to 0°, which includes part of the equatorial and mid-latitude region of the moon's southern hemisphere (Fig. 1); our mapping thus characterizes the type and extent of terrains and geological processes representative of this locale. We used Cassini's RADAR data, acquired in the Synthetic Aperture Radar (SAR) mode as our basemap, supplemented by secondary datasets such as microwave emissivity and topography from RADAR-derived datasets, and infrared reflectance from the Imaging Science Subsystem (ISS) and the Visual and Infrared Mapping Spectrometer (VIMS) to provide additional constraints on our terrain assignment.

This study is a continuation of the detailed geomorphological mapping effort introduced in Malaska et al. (2016a). In Lopes et al. (2020), we present a global Titan map that is related to the detailed mapping of Malaska et al. (2016a) and the work presented here, but at a coarser scale. The characterization and description of mapping units discussed in this paper will follow previously established conventions. We chose to follow up our detailed mapping of the Afekan Crater region with a detailed map of the South Belet region for several reason. First, the South Belet region, which spans Titan's equatorial and southern mid-latitudes, works as a natural corollary to the characterization of Titan's equatorial and northern mid-latitude regions performed with the Afekan map; questions of latitudinal dependence, symmetry, and regional variations can be readily investigated and expanded towards broader conclusions of Titan's geologic history. Second, this first detailed map of South Belet leads to the identification of new terrain units and to the discussion of previously unidentified geologic processes characteristic of the equatorial and mid-latitude regions. Third, South Belet features interaction between dune and non-dune units, especially at the sand sea boundaries, that allows for investigating the connection between these units, and can be compared to northern hemisphere mapping in Afekan.

2. Geologic setting

The areal extent of South Belet amounts to 9.5×10^6 km^2, or 11.3% of Titan's surface. SAR swaths provide 31.8% coverage of the region at high resolution (260–500 m/pixel), which accounts for about 3.6% of Titan's surface. From initial examination of the global map presented in Lopes et al. (2020), and much like the Afekan Crater region of Titan as discussed in Malaska et al. (2016a), South Belet appears typical of Titan's mid-latitude and equatorial regions. The region most notably contains the Belet Sand Sea, located on Titan's trailing hemisphere between 30°S and 25°N latitude and 60° and 120°E longitude, and is in a topographically low basin with an average elevation of approximately −300 m (Le Gall et al., 2011; Corlies et al., 2017). As mentioned, Belet is the largest sand sea on Titan, with an estimated area of 3.3 ± 0.6 million km^2 and estimated sand volume of 610,000 to 1,270,000 km^3 (Le Gall et al., 2011). The South Belet region contains one unnamed crater of suitable certainty (Hedgepeth et al., 2020). Like Titan's Afekan Crater region, South Belet's equatorial sand sea is in contact with large expanses of the featureless plains, where the transition from dunes to plains starts roughly at the 20°S latitude line. Lopes et al. (2020) shows that plains dominate Titan's mid-latitudes globally; the conspicuous lack of SAR coverage beyond this latitude line (notably from 25°S to 60°S; see Fig. 2) may result in the underestimation of the total area of the plains (and associated subunits) in this region.

The detailed mapping was predominately performed using the SAR dataset on areas where coverage is available. We follow the procedure described in Malaska et al. (2016a) and distinguish between discrete units based on radar backscatter and overall morphology. We also considered feature geometry, sharpness of boundaries, internal texture, degree of dissection, and overall context when ultimately assigning a terrain classification. Differences in Cassini SAR images represent differences in signal returned to the spacecraft. The returned signal, or "backscatter", can be a result of a change to any of a number of properties, such as incidence angle of the beam, slope angle orthogonal to the beam, surface roughness, volume scattering, structural properties, subsurface inhomogeneities, and dielectric constant of the material. A difference in backscatter can be a result of a change to any one of these properties. Other RADAR modes, such as radiometry (e.g., Wye et al., 2007; Janssen et al., 2009, 2011, 2016) and altimetry (e.g., Kirk et al., 2005; Stiles et al., 2009), provide supplementary information about the surface. We use data from these modes, in addition to observations of visual reflectance from ISS and infrared from VIMS, to further refine our mapping delineations and make final terrain assignments.

3. Methods

3.1. Datasets and instruments

3.1.1. SAR

Due to the absorptive and scattering nature of Titan's atmosphere, the efficacy of detailed visual and infrared spectro-imaging, normally used in planetary remote sensing, is limited. Methane absorbs mostly in

the infrared, while Titan's haze layers scatter light at the visible to near-infrared parts of the spectrum. As a result, the multimode RADAR instrument (Ku-band, 13.78 GHz, $\lambda = 2.17$ cm; Elachi et al., 2005a,b, 2006) was the main instrument used to study Titan's geomorphology. We used data from the SAR mode as our primary basemap, using backscatter return to define the boundaries and create the main categorization schema for our terrain units.

The SAR mode operates mostly at altitudes under ~4000 km, yielding image resolutions from 260 m/pixel to 500 m/pixel, with the best resolution acquired in the center of the swath during closest approach. SAR data cover about 46% of Titan's surface at less than 1 km resolution, while the higher-altitude SAR data cover an additional 24% at less than 5 km resolution (Lopes et al., 2020). Each swath is 120 to 450 km wide, and 1000 to 5000 km long. For mapping purposes, we used incidence angle corrected SAR swaths to minimize geometric variations. A SAR mosaic of the South Belet region is shown in Fig. 2, and includes SAR swaths from flyby's T8, T19, T21, T49, T50, T57, T61, T84, and T92. Materials having high-backscatter appear lighter in the images, while materials having low-backscatter appear darker.

3.1.2. Topography

Topographic information can be obtained from overlapping SAR beams by SARTopo (Stiles et al., 2009). SARTopo provides 1 to 3 profile strips per SAR pass. Each strip is 10 km wide and thousands of kilometers long with vertical uncertainties of <75 m. Relative elevation information is, in general, only valid along the same SARTopo strip, and thus we refrain from comparing strips generated from different SAR swaths. The Cassini RADAR instrument also had a dedicated altimetry mode that provided limited, but higher-resolution (~35 m), elevation data. However, altimetry cannot be obtained simultaneously with SAR and thus covers relatively small segments of the surface. For our purposes, we use an updated topographic map of Titan generated by Corlies et al. (2017) that includes all SARTopo, altimetry, and stereophotogrammetry topographic data available at the end of the Cassini mission. A SAR mosaic coverage with superimposed SARTopo strips for South Belet is shown in Fig. 3.

3.1.3. Emissivity

The RADAR instrument had a passive radiometry mode that measured the brightness temperature of the surface of Titan (Janssen et al., 2009, 2016). The brightness temperature is converted to emissivity (E) using Titan's surface temperature (~95 K in the equatorial regions) (Fulchignoni et al., 2005; Jennings et al., 2016). Radiometry resolution varies from 5 to 500 km, with higher resolution data corresponding directly to SAR swaths (i.e. when the spacecraft was closest to Titan). Materials having low emissivity are interpreted as fractured water ice, whereas materials having high emissivity are interpreted as organic (Janssen et al., 2016). An emissivity map of the South Belet region is shown in Fig. 4.

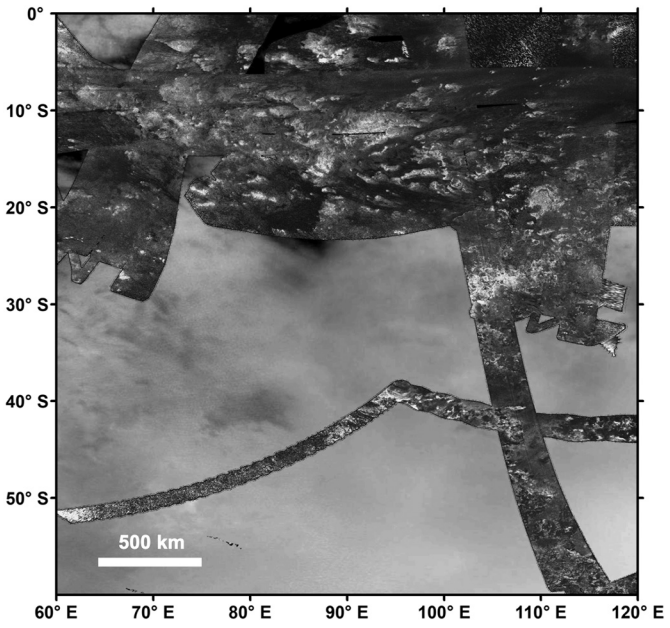

Fig. 2. The South Belet Region as seen in our SAR mosaic base map. The SAR mosaic is superposed on a globally controlled ISS mosaic. See text for details.

3.1.4. ISS and VIMS

Cassini's Imaging Science Subsystem (Porco et al., 2004) had Wide and Narrow Angle Cameras that included 0.938-μm filters and infrared polarizing filters capable of imaging Titan's surface through an

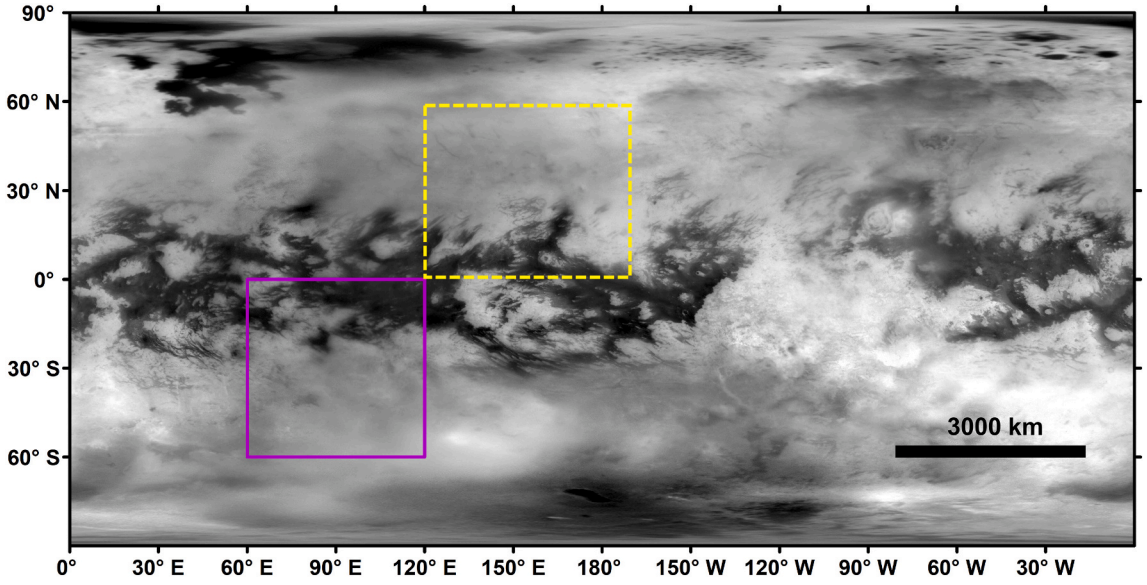

Fig. 1. Global context of the South Belet Region (purple box) on an Imaging Science Subsystem (ISS) mosaic (Karkoschka et al., 2017). The Afekan Crater region (Malaska et al., 2016a) is also indicated for reference (yellow, dashed box). (For interpretation of the references to colour in this figure legend, the reader is referred to the web version of this article.)

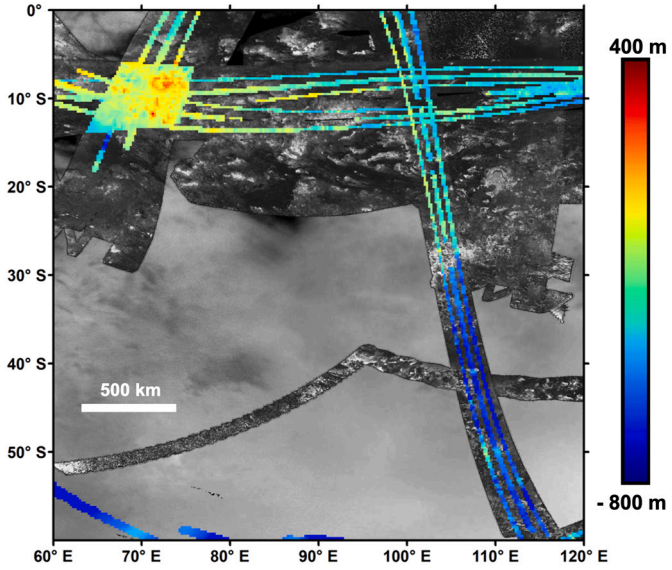

Fig. 3. SAR plus ISS mosaic with SARTopo overlay for the South Belet Region with data obtained from Corlies et al. (2017).

atmospheric transmission window. At best, the theoretical spatial resolution of these images is several hundred meters, but this theoretical resolution is severely degraded by the strong scattering of the atmosphere. We used a global controlled and corrected ISS mosaic at ~1 km resampled pixel-scale for our mapping (Karkoschka et al., 2017; Fig. 5).

Cassini's VIMS instrument (Brown et al., 2004) was a hyperspectral mapping spectrometer that then observed Titan's surface through atmospheric transmission windows at 0.94, 1.08, 1.28, 1.58, 2.03, 2.69, 2.79, and 5.0 μm (Sotin et al., 2005; Barnes et al., 2007a). VIMS data provide constraints on the composition of the surface (e.g., Soderblom et al., 2007; Brown et al., 2008; Clark et al., 2010; Solomonidou et al., 2014, 2018, 2020a; Brossier et al., 2018; Griffith et al., 2019). VIMS pixel-scale typically ranges from a 0.5 km to tens of km, but only 5% of the surface was observed by VIMS at a resolution of <5 km/pixel (Le Mouélic et al., 2019). For a very small number of targeted areas observed during closest approach, the scale can be as high as 500 m/pixel (Jaumann et al., 2009). The global VIMS mosaic described in Le Mouélic et al. (2019) and locally merged with ISS (Seignovert et al., 2019), cropped for South Belet, is shown in Fig. 6.

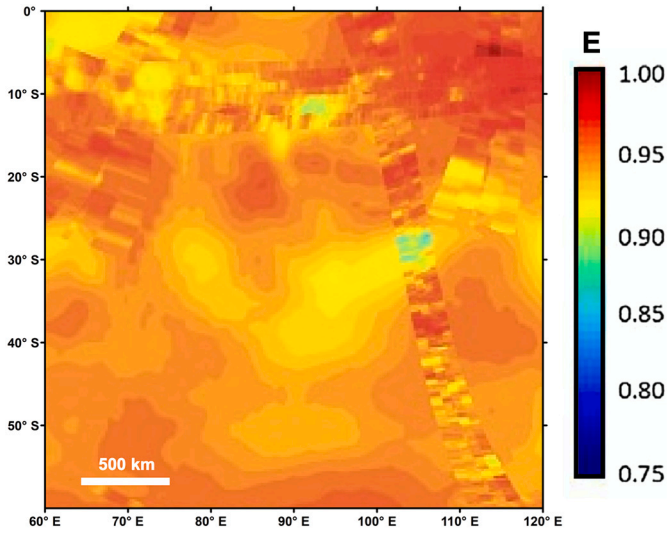

Fig. 4. Emissivity map of the South Belet region. Data from Janssen et al. (2016).

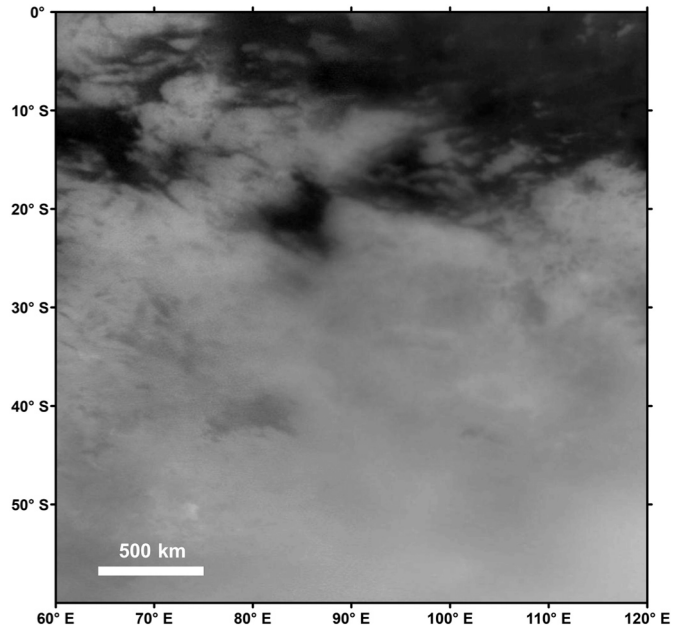

Fig. 5. ISS mosaic of the South Belet region.

3.2. Mapping technique

SAR mosaics were loaded into ArcGIS™ 10.6 (ESRI) software package, then used as the base layer data for morphological classification. We drew contacts between terrains of different radar backscatter or morphological texture. We determined terrain boundaries following previous studies (e.g., Stofan et al., 2007; Lopes et al., 2010; Williams et al., 2011; Malaska et al., 2016a). In general, we only use the higher-resolution SAR swaths for mapping and mapped at an image scale of

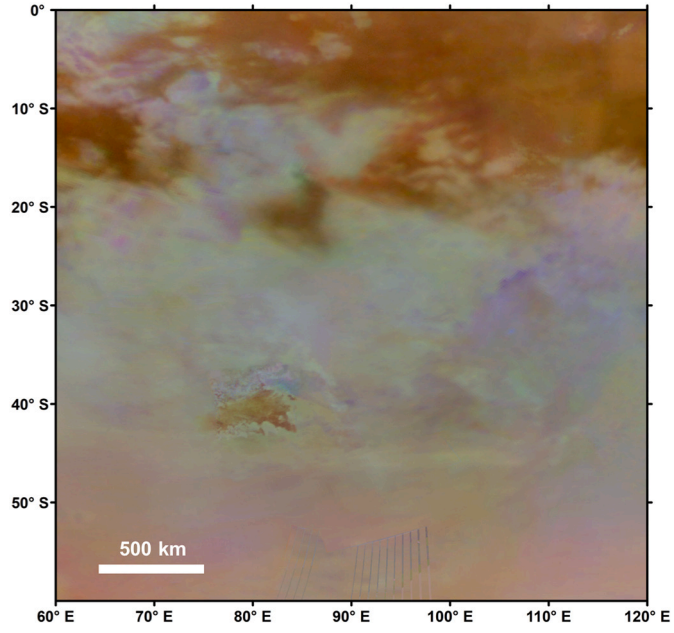

Fig. 6. VIMS mosaic of South Belet. The mosaic is made from a combination of a VIMS haze corrected dataset (at first order, see Le Mouélic et al., 2019) and ISS (from Seignovert et al., 2019). RGB composite is 1.59/1.27 μm (red), 2.03/1.27 μm (green) and 1.27/1.08 μm (blue) corrected from atmospheric scattering as described in Le Mouélic et al. (2019). (For interpretation of the references to colour in this figure legend, the reader is referred to the web version of this article.)

1:800,000 (Greeley and Batson, 1990). However, in certain areas, HiSAR (a high-altitude SAR imaging mode with km to multi-km scale resolution) of sufficient quality was included in the base map and used for mapping. We determined if a HiSAR swath was of suitable quality based on the capacity to distinguish terrain units with the same level of detail as with a regular SAR swath. For example, a HiSAR swath was included in our mapping if we were able to distinguish between "undifferentiated plains", "variable featured plains", "hummocky", and "linear" or "featureless" dunes; an example area mapped with HiSAR is centered on 18.1°S, 89.5°E. In total, 4.6% of the mapped area was done so with HiSAR. SAR or HiSAR swaths that were too low resolution, either because of noise or large pixel-scale, were not used for primary identification. We defined gradational contacts between units if a clear delineation could not be made at the resolution of the SAR images. Polygons were generated from the drawn contacts using ArcGIS functionalities; these polygons were then assigned a terrain unit classification based on feature morphology and radar backscatter. Data from SARTopo, radiometry, ISS, and VIMS were used to refine terrain classification as outlined in Malaska et al. (2016a).

4. Description of map units

The terrain classes and units in the South Belet region were identified using the SAR mosaic basemap. While there are six major terrain classes on Titan, four of these are found in the South Belet region. These are: plains, dunes, hummocky/mountains, and craters. We did not observe any terrain units belonging to the Lake and Basin or Labyrinth terrain classes. Each terrain class was subdivided into terrain units by characteristic morphology (texture, border geometry, and general appearance) and radar backscatter. Radar backscatter is broadly classified as "high", "medium", "low", and in some cases as "variable". Physical features such as crater rims and channels were added as separate polyline layers to our map. Channel mapping is based on procedure described in Burr et al. (2013a). The map is shown in Fig. 7, and a graphic of physical features is shown in Fig. 8.

Many of the units identified in the South Belet map are described in detail in Malaska et al. (2016a) and have been used for the VIMS analysis of various Titan areas in Solomonidou et al. (2018); rather than repeat those descriptions here, we provide a summary in Table 1. The three-letter terrain unit abbreviations refer to the broad terrain class (e.g., *p* for plains), a descriptor letter for the terrain type (e.g., *u* for undifferentiated), and a letter indicative of relative radar backscatter (e.g., *l* for low) (Malaska et al., 2016a). We also present local examples for each unit in SAR, which are shown in Fig. 9.

We found two terrain units that were not included in Malaska et al. (2016a) that were identified in our mapping of South Belet. In the following section we describe and discuss these terrain units.

4.1. Bright alluvial plains (pah)

Description. The bright alluvial plains (*pah*) are radar bright, triangular shaped features typically found at the terminus of observable channel structure (Fig. 10). These features have sharp to diffuse boundaries, with backscatter tending to decrease away from the apex of the triangle. These regions have low emissivity, much lower than other plains units like variable (*pfv*), undifferentiated (*pul*), and scalloped (*psv*). In some cases, the *pah* unit appears to have microwave emissivity characteristics similar to the mountain/hummocky units. They are more commonly found at higher latitudes and are commonly associated with nearby mountainous terrain or other local topographic highs. *Type area:* 28.6°S, 105.2°E.

Interpretation. These features are interpreted as alluvial deposits of high backscatter materials emplaced by fluvial activity. A global survey of Titan's alluvial fans is given in Birch et al. (2016) and Radebaugh et al. (2018) and includes the fans identified here. Fans on Earth similarly show higher backscatter compared to their surroundings as well as

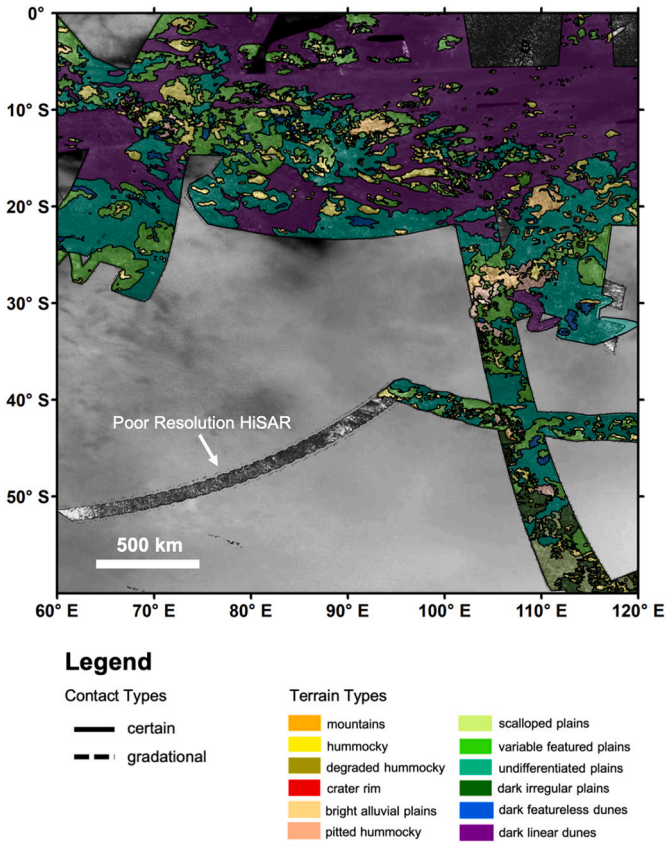

Fig. 7. Geomorphological map of the South Belet region, including the major geomorphological units.

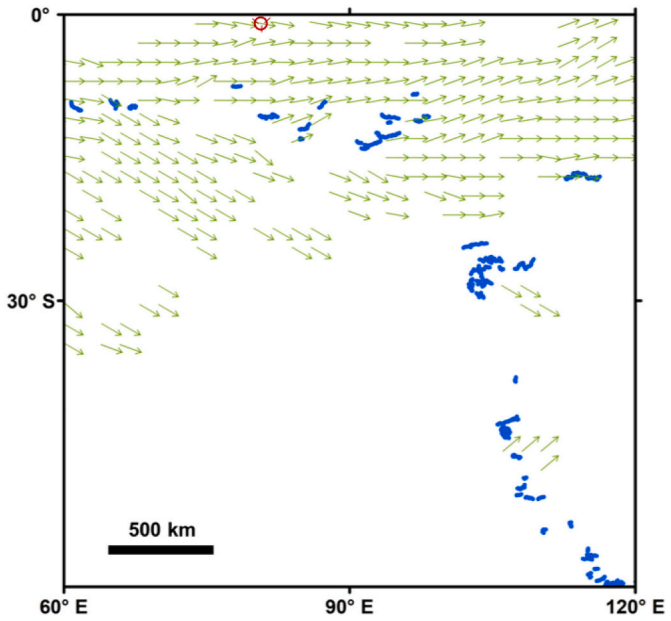

Fig. 8. Potential valleys, channels, and crater rims of the South Belet region and possible material transfer on the surface. The green arrows represent inferred material transport directions from Malaska et al. (2016b). Blue lines indicate valley and channels, while red solid circles indicate crater rims, respectively. (For interpretation of the references to colour in this figure legend, the reader is referred to the web version of this article.)

Table 1
Terrain units identified in Titan's South Belet region. Unit description and interpretations, with the exception of *hph* and *pah*, summarized from Malaska et al. (2016a). The three-letter terrain unit abbreviations refer to the broad terrain class (e.g., p for plains), a descriptor letter for the terrain type (e.g., u for undifferentiated), and a letter indicative of relative radar backscatter (e.g., l for low).

Terrain class	Terrain Unit Name	Terrain Unit Code	Local type location	Terrain Unit Description	Interpretation
Crater	Crater rim	*crh*	0.023°N, 79.51°W	High-backscatter hummocky or mountainous terrain in a circle with clear dissection on inside edge	Impact crater rim
	Crater ejecta	*ceh*	0.039°S, 80.03°E	Rough, radar-bright to radar-medium material that grades away radially from a rim	Impact crater ejecta
Mountains/Hummocky	Mountain	*hm*	11.55°S, 92.52°E	Elongated features with evident SAR bright/dark pairing	Rugged mountainous areas of ancient crust
	Hummocky	*hh*	3.54°S, 72.72°E	Radar-bright "blob" like exposures; unclear bright/dark pairing	Highland areas of ancient crust
	Degraded hummocky	*hdm*	19.57°S, 116.56°E	Small exposures of hummocky-like materials with comparatively lower backscatter return	Small remnants of hummocky terrains eroded or partially buried by organics
	Pitted hummocky	*hph*	11.7°S, 71.4°E.	Radar-bright hummocks populated by radar-dark, pit-like structures	Fine grained, low backscatter materials deposited in pre-existing depressions in the exposed icy crust
Plains	Bright alluvial deposit	*pah*	28.23°S, 105.01°E	Radar-bright, triangular shaped regions typically found at the terminus of channel; backscatter decreases away from apex of triangle	Alluvial deposits originating from fluvial activity
	Undifferentiated plains	*pul*	22.85°S, 65.78°E	Low backscatter nearly featureless plains; most extensive unit on Titan, dominate the mid-latitudes	Deposits of organic, aeolian-transported materials
	Variable featured plains	*pfv*	13.21°S, 74.48°E	Plains of variable backscatter, with characteristic internal texture. Terminates at diffuse boundaries.	Deposits of eroded materials from mountain and hummocky units
	Dark irregular plains	*pil*	50.97°S, 108.63°E	Irregular patches of radar-dark, lobate terrain set in a low-to-medium backscatter substrate	Low-lying basins dampened by liquids or muds
	Scalloped plains	*psv*	56.85°S, 111.45°E	Extensive units mostly at high latitudes; medium backscatter, with scalloped borders and patchy internal structure	Eroded hummocky terrains partially covered by organic materials or potentially evaporitic remnants of previously filled lake basins
Dunes	Featureless sand sheets	*ds*	11.93°S, 84.32°E	Featureless radar-dark areas extending in patches consistent with aeolian transport direction	Sand deposits that may contain dune structures below the resolution of radar
	Linear dunes	*dl*	7.64°S, 93.03°E	Parallel to sub-parallel radar-dark lineations on a variable backscatter substrate	Dunes, mostly longitudinal, composed of organic materials

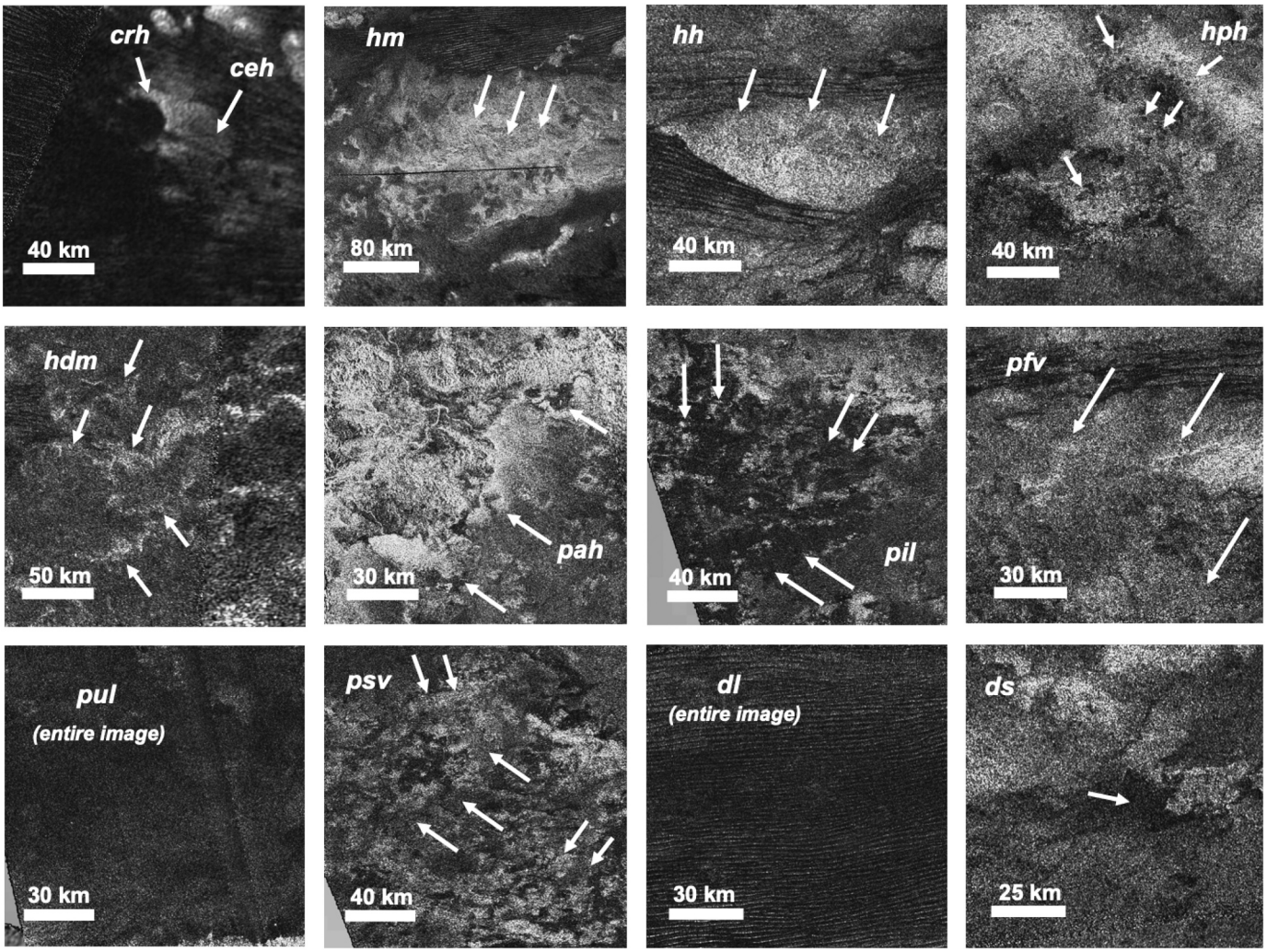

Fig. 9. Example of units identified in South Belet, presented as SAR images. White arrows point to the representative feature. With the exception of the *pah* and *hph* units, all units, including local type examples, are previously discussed in Malaska et al. (2016a). Units are: *crh* = crater rim, *ceh* = crater ejecta, *hm* = mountain, *hh* = hummocky, *hph* = pitted hummocky, *hdm* = degraded hummocky, *pah* = bright alluvial plains, *pil* = dark irregular plains, *pfv* = variable featured plains, *pul* = undifferentiated plains, *psv* = scalloped plains, *dl* = linear dunes, *ds* = featureless sand sheets.

radar darkening away from the fan apex (Schaber et al., 1976; Birch et al., 2016). High backscatter of the fans in SAR images may be due to either grains with a size comparable to the SAR wavelength, 2.2 cm (Le Gall et al., 2010; Schaber et al., 1976), or to high porosity in the top few meters of the deposit causing additional scattering (Birch et al., 2016). Grains (pebbles and cobbles) of this size were imaged at the Huygens landing site (Tomasko et al., 2005).

The low microwave emissivity response (Fig. 10d) is likewise consistent with volume scattering from subsurface inhomogeneities (Paganelli et al., 2008), such as a loosely consolidated mix of water ice and organic sediments. Both the VIMS and ISS maps (though more pronounced in VIMS) show albedo differences between the area southeast of the mountainous unit (*hm*) and adjacent terrain (Fig. 10e,f). This area corresponds to the location of the bright alluvial plains and the channels. The dark-blue unit in VIMS has been associated with channels (e.g. Barnes et al., 2007b; Langhans et al., 2012). We thus find that the VIMS observation may be showing an "icy sediment" transport direction for the highlighted region, consistent with the presence of the channels and alluvial plain unit. Similarly, Brossier et al. (2018) recently showed trends in water ice content and grain size properties of the VIMS blue unit within transition zones between infrared bright-blue-brown units that support the fluvial origin of these deposits.

4.2. Pitted hummocky

Description. Pitted hummocky terrain (*hpm*) units are similar to hummocky (*hh*) terrain in that they are high-backscatter areas with rounded boundaries and internal textures varying from uniform to "lumpy". They are different from hummocky terrains in that they are "pitted" by dark circular features 1 to 6 km in diameter (Fig. 11). However, smaller, sub-resolution pits may be present. A pitted hummocky feature maybe be partially or completely marked by these dark features. The microwave emissivity is somewhat higher than that of the hummocky terrain unit (*hh*), but lower than the surrounding plain units, and the SARTopo is consistent with these being terrains that are locally elevated. Similar features of this specific morphology (Fig. 11f), assumed to be depressions or pits, were first identified by Lopes et al. (2007) within Cassini's T8 swath. *Type area:* 11.7°S, 71.4°E.

Interpretation. We interpret this unit as elevated areas of ancient crust, similar to our interpretation of the hummocky terrain unit. However, we speculate that the dark quasi-circular features within these exposures are topographic depressions filled with low backscatter materials, though we have no detailed topographic information that supports this. The microwave emissivity data of this terrain is similar to that of the hummocky terrain and suggests that the pitted hummocky terrains consist of fractured water ice or water ice and organic material

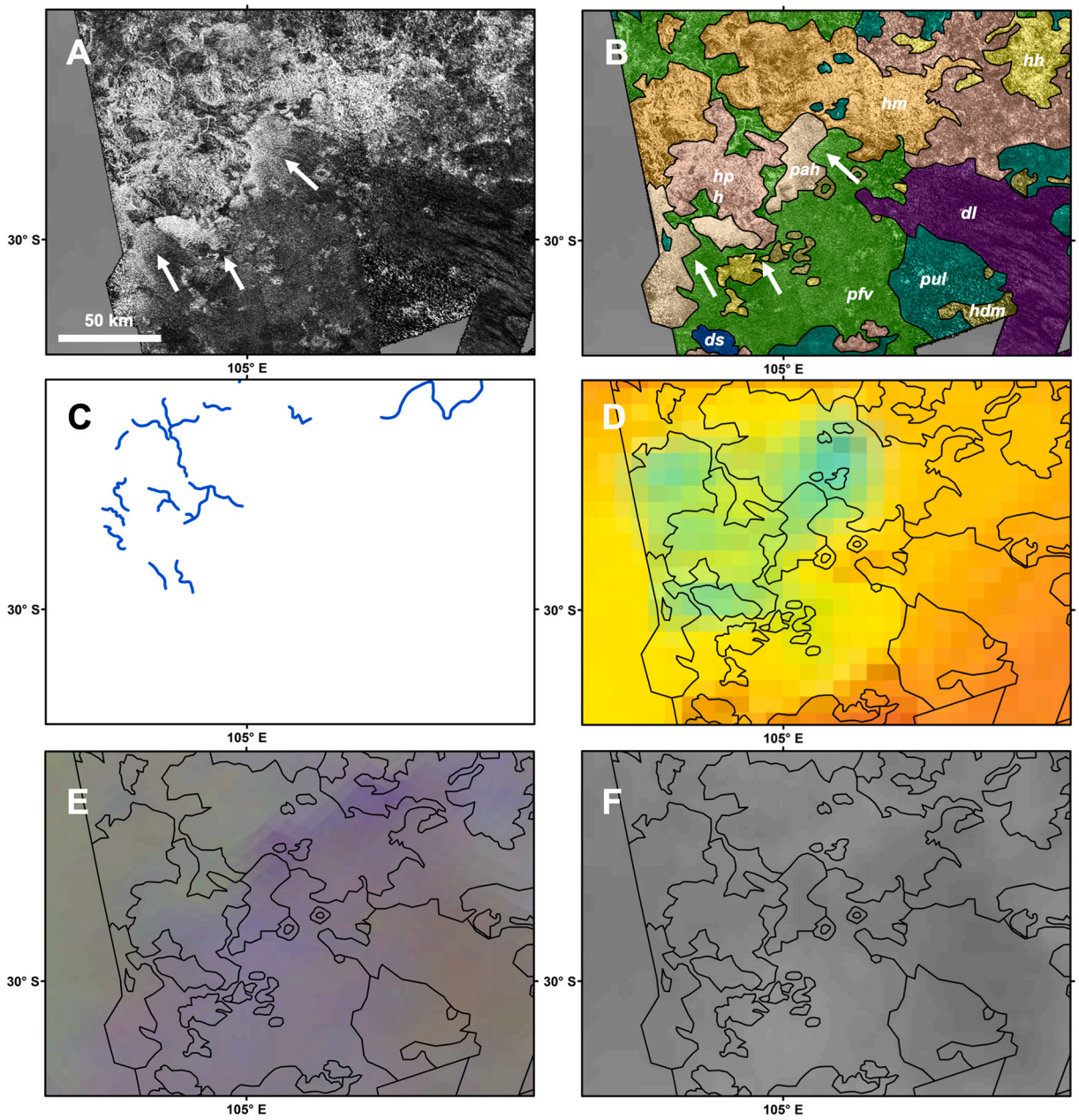

Fig. 10. Instances of bright alluvial plains (28.6°S, 105.2°E): (A) SAR mosaic, bright alluvial plains indicated by white arrows. (B) Annotated terrain unit mapping on the SAR mosaic. (C) Channels that terminate in the bright alluvial plains indicated via a blue line (detail from Fig. 8). (D) Emissivity map with contacts between terrain units shown. See Fig. 4 for color scale. (E) VIMS RGB mosaic with contacts between terrain units outlined. (F) ISS mosaic with contacts between terrain units shown. (For interpretation of the references to colour in this figure legend, the reader is referred to the web version of this article.)

mixtures. It is not possible, given the resolution of the microwave emissivity dataset, to determine if the dark pits are radiometrically distinct from their host hummocky structures. In addition, the low resolution of VIMS compared to the other data does not allow for an individual study of the dark quasi-circular features. The topographic expression of the pits likewise cannot be resolved given the resolution of the SARTopo data. A more detailed discussion of the pits, including possible formation scenarios, is explored in Section 5.5.

5. Geologic synthesis

5.1. Comparing South Belet to Afekan and the global map

Table 2 quantifies the mapping done in South Belet, and Table 3 compares the areal extent of the terrain units in South Belet to Afekan and to the global map. Much like in the case of the Afekan region, our mapping shows that plains are the most widespread type of terrain unit in South Belet, comprising 46.6% of the mapped area (Table 2). Unlike Afekan, the dunes closely rival the dominance of plains, making up 43.0% of the mapped area. The areal extent of dunes for Afekan (18.6%) is comparable to the spatial extent of dunes from the global map (17.0%), making South Belet uncharacteristically dominated by dune units. However, this may be an observational bias caused by lack of SAR coverage beyond South Belet's equatorial belt, underrepresenting the plains units that are more likely to be found south of the 30-degree latitude line. At the same time, South Belet hosts a large portion of the Belet Sand Sea, so it is reasonable to expect a larger representation of the dune units.

The next most prominent unit are the mountains/hummocky terrains (10.4%), percent-wise similar to Afekan (11.5%) and the global map

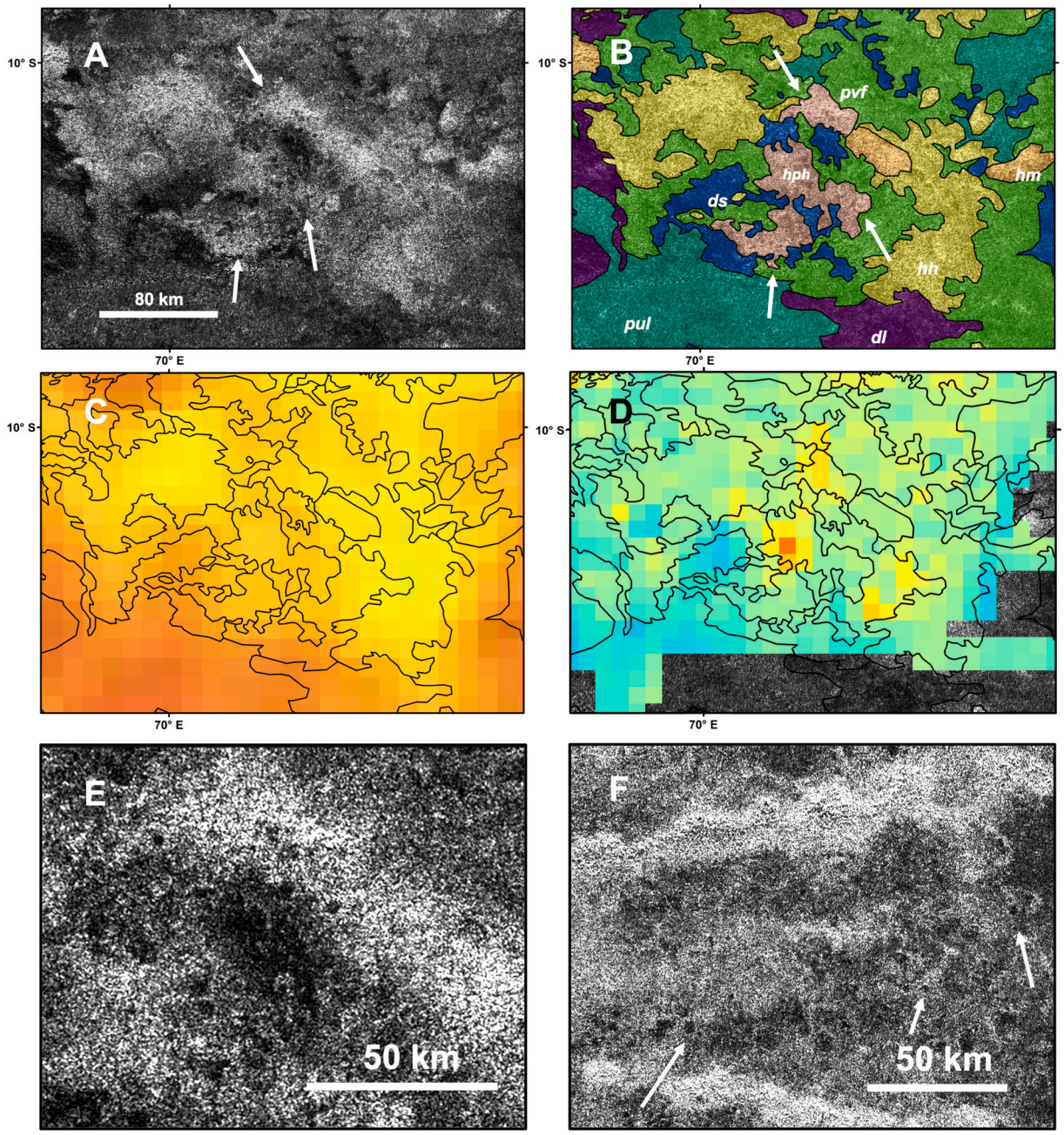

Fig. 11. Example of pitted hummocky terrain (*hph*) (11.7°S, 71.4°E): (A) SAR mosaic, pitted hummocks indicated via white arrows. (B) Annotated terrain unit mapping on a SAR mosaic. (C) Emissivity map overlain with contacts between terrain units. See Fig. 4 for color scale. (D) Topography of the pitted hummocky terrain interpolated from closely overlapping SARTopo bands. See Fig. 3 for color scale. (E) Zoom-in on the pitted hummocky patch indicated by the topmost white arrow in A. (F) SAR mosaic of pitted hummocky terrain (*hph*) in Adiri, indicated by white arrows (8.8°S, 138.8°E).

(14.0%). And finally, the crater terrain units (0.01%) are the least prominent unit in South Belet. There are no labyrinth units identified in South Belet, whereas labyrinths make up 2.3% of area coverage in Afekan, and 1.5% areal coverage of the global map. South Belet also contains no basin and lake units. The Malaska et al. (2016a) paper reported no basin and lake units in Afekan. However, after reevaluating the map post-publication, we revised mapping in the higher latitudes to include "sharp-edged depressions" (*bse*) and have since identified 5 *bse* units within existing units, mainly the undifferentiated plains and the scalloped plains.

In South Belet, the undifferentiated plains (*pul*) comprise 27.5% of the entire mapped area and are spatially the most dominant of the plain units, though not as dominant as the undifferentiated plains in Afekan, which comprise 46.0% of the entire area in that region. Variable featured plains (*pfv*) are the second most widespread plains unit, making up 16.8% of the entire mapped area, followed by "dark irregular plains" (*pil*; 1.3%), "scalloped plains" (*psv*; 0.8%), and then "bright alluvial deposit" (*pah*; 0.1%). "Lineated plains" (*plh*) and "streak-like plains" (*psh*), which were identified in Afekan, are not seen in South Belet. In the case of the dunes units, linear dunes (*dl*), primarily from the Belet dune seas, make up the majority (41.5%), whereas featureless sand sheets (*ds*) covers a relatively small area (1.5%). There were no mapped occurrences of the reticulated dune units (*dt*), whereas 0.3% of mapped dunes in Afekan are reticulated.

The hummocky (*hh*) unit (582 identified) make up the bulk of terrain exposures. Variable feature plains (*pfv*) were also widespread (221

Table 2
Terrain unit statistics in the South Belet region.

Terrain class	Terrain Unit Name	Total Area (km^2)	Number of Feature	Average Size (km^2)	% of mapped area	% mapped per class
Crater	Crater rim (*crh*)	78	2	39	<0.1	0.01
	Crater ejecta (*ceh*)	213	2	106	<0.1	
Mountains/hummocky	Mountain (*hm*)	50,160	25	2006	1.6	10.36
	Hummocky(*hh*)	251,347	582	431.87	8.1	
	Degraded hummocky (*hdm*)	19,747	88	224	0.6	
	Pitted hummocky (*hph*)	779	3	260	<0.1	
Plains	Bright alluvial deposit (*pah*)	2841	2	1420	0.1	46.63
	Undifferentiated plains (*pul*)	852,917	99	8615	27.5	
	Variable featured plains (*pfv*)	521,826	221	2361	16.8	
	Dark irregular plains (*pil*)	38,774	69	38,774	1.3	
	Scalloped plains (*psv*)	25,278	8	3160	0.8	
Dunes	Featureless sand sheets (*ds*)	47,207	110	429	1.5	43
	Linear dunes (*dl*)	1,286,125	16	80,383	41.5	

Table 3
Percentage of areal extent of units in South Belet compared to Afekan (Malaska et al., 2016a) and the global map (Lopes et al., 2020).

Terrain Unit	South Belet	Afekan	Global Map
Crater	*<0.1*	*0.8*	*0.4*
Crater rim (crh)	<0.1	0.3	
Crater ejecta (ceh)	<0.1	0.5	
Crater fill 2 (*cf2*)	–	<0.1	
Crater fill 1 (*cf1*)	–	<0.1	
Central peak (*cph*)	–	<0.1	
Hummocky	*10.36*	*11.5*	*14*
Mountain (*hm*)	1.6	4.2	
Hummocky (*hh*)	8.1	4.9	
Degraded hummocky (*hdm*)	0.6	1.3	
Pitted hummocky (*hph*)	0.1	–	
Cross-cut hummocky (*hxh*)	–	1.1	
Labyrinth	–	*2.3*	*1.5*
Plains	*46.63*	*66.8*	*65*
Bright alluvial deposit (*pah*)	0.1	–	
Undifferentiated plains (*pul*)	27.5	46	
Variable featured plains (*pfv*)	16.8	13.4	
Dark irregular plains (*pil*)	1.3	0.5	
Scalloped plains (*psv*)	0.8	1.5	
Lineated Plains (*plh*)	–	0.4	
Dunes	*43.0*	*18.6*	*17*
Featureless sand sheets (*ds*)	1.5	2.2	
Linear dunes (*dl*)	41.5	16.1	
Reticulated dunes (*dr*)	–	0.3	

identified), followed by featureless sand sheets (*ds*; 110 identified). Hummocky terrain units are widespread yet fairly small in areal extent, with an average size under 500 km^2. However, the linear dunes, mainly part of the contiguous Belet sand sea, are extensive, with the average size of an individually mapped dune area being roughly 81,000 km^2 (about 1.5 times larger than the average size of linear dune terrain units in Afekan). The average size of an individual unit of undifferentiated plains (~ 8600 km^2, compared to 21,000 km^2 for Afekan) may be an underestimate, especially because greater radar coverage in the southern half of the South Belet region would likely connect isolated units in individual swaths into larger expanses of the unit.

Crater units, limited to crater rim and ejecta, comprise less than 0.1% of the mapped surface in South Belet, compared to 0.8% for Afekan. Crater units are interpreted as the direct result of impact processes. Previous work (Werynski et al., 2019; Solomonidou et al., 2020a) suggests that evidence of impacts have been erased by other geological processes, likely those that form dunes and plains. When compared to Afekan, which features 17 exposures of crater related units, South Belet is particularly deficient, featuring only 4. This is likely owing to both spatial coverage bias (especially in areas away from dunes) and burial or fill potential within the Belet sand sea (e.g. Neish et al., 2013; Hedgepeth et al., 2020). While it is possible to use the ISS or VIMS mosaic to identify crater rims, none are found in either within the South Belet region. If there are any craters outside the SAR boundaries, it is possible that they are too small or too low contrast to be seen in ISS or VIMS. There is only one identified crater in South Belet that is unnamed; we identify 4 crater-like features with potential impact origins as well, but they are insufficiently resolved to confidently describe as such.

South Belet is likewise deficient in the "labyrinth" terrain unit described in Malaska et al. (2016a, 2020) suggesting either that the process behind the formation of these units has not taken place in this area, or that they have since been completely eroded/buried. It is also possible, given the preferential distribution of labyrinth at high latitudes (Malaska et al., 2020), that the aforementioned lack of SAR coverage in these latitude regions has left these units unidentified. The SAR in this region is largely deficient south of the 30° latitude line, and labyrinths are normally found north of the 30°N line or south of the 30°S line (Malaska et al., 2020). However, ISS images will sometimes show a subtle darkening that corresponds to the presence of labyrinth terrains within surrounding plains units, although this was not considered a defining characteristic due to the fact that not all labyrinths are visible in ISS. Similarly, darkening in ISS images can correlate to other terrains, and none of that seen in South Belet region outside the bounds of the SAR can be assuredly labeled as labyrinth.

Next, we briefly discuss the characteristics of South Belet's mid-latitude-to-pole transition region (~50°S to 60°S) and compare it to the transition regions of Afekan and Soi, both of which are located in Titan's northern hemisphere. There are two units in particular that seem to define the morphology of Titan's transitional zones and have been identified in our mapping in the northern hemispheres (Malaska et al., 2016a; Lopes et al., 2020) and here in the southern hemisphere: the scalloped plains (*psv*) and the dark irregular plains (*pil*). For descriptions of these two units, see Table 1.

In the Afekan region, a small portion of scalloped plains is observed in the northwest region of that study area (Fig. 12), making up 1.5% of the mapped area (Malaska et al., 2016a). In the Soi region, a similarly sized portion of scalloped plains is also observed in the northernmost part of the study area (Lopes et al., 2019) and makes up 1.6% of that mapped area. VIMS analysis showed the scalloped plains as one of the highest albedo terrain units on Titan (Solomonidou et al., 2018). Following Malaska et al. (2016a), we have interpreted this terrain unit as composed of either organic materials that are slightly higher in radar backscatter than the undifferentiated plains, or else as eroded hummocky materials that have been covered by a relatively thin layer of organics. The scalloped plains begin to appear around latitudes of 50°S and extend toward the poles; they correlate well with the mottled plains (Vm_b) and uniform SAR-bright plains (Vu_b) terrain unit classifications described in Birch et al. (2017). In higher latitude regions, small, empty depressions can be seen within this unit (Lopes et al., 2020) that are similar in morphology to the empty sharp-edged depressions (SEDs)

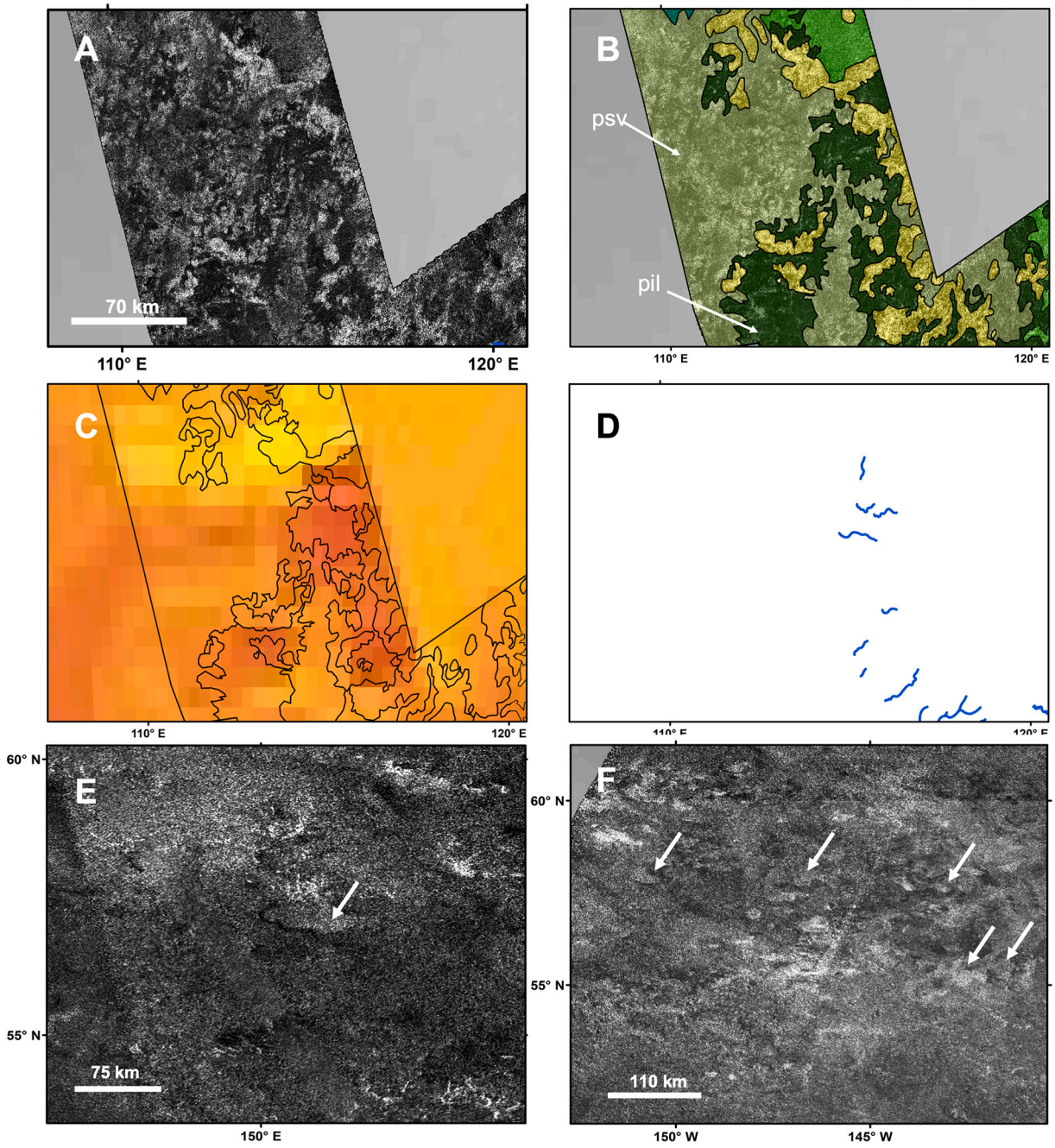

Fig. 12. Region south of the 50°S line in South Belet, presented in sinusoidal projection. (A) SAR mosaic. (B) Annotated terrain map on the SAR mosaic with scalloped plains (*psv*) and dark irregular plains (*pil*). (C) Microwave emissivity map. (D) Location of channels in area, marked in blue. (E) SAR mosaic of the transition zones in Afekan, and (F) Soi. White arrows indicate sharp edge depressions (*bse*), interpreted as empty lakes. (For interpretation of the references to colour in this figure legend, the reader is referred to the web version of this article.)

(Birch et al., 2017; Hayes et al., 2017) (Fig. 12E and F). Identification of SEDs is more ambiguous in South Belet; there are some features reminiscent of SEDs, such as topographic lows (relative to surrounding terrain) corresponding to radar bright floors, but the quality of the SAR data in this area makes it difficult to definitively label it as such.

South Belet's scalloped plains are also patchier when compared to Afekan and Soi; South Belet has a smaller average size per feature (3200 km^2) when compared to Afekan (22,000 km^2) and Soi (98,000 km^2). This may also be due to a bias in spatial coverage for the higher latitudes, and the scalloped plains we are observing may be skewing small due to an insufficient sample size. South Belet's transitional latitude similarly differs from that of Afekan and Soi in that there are more channels in contact with the scalloped plains and dark irregular plains units within the latitude zones under consideration (Fig. 12d); there is 1 channel mapped north of the 50°N latitude line in Soi, zero channels mapped north of the 50°N latitude line in Afekan, and 17 mapped channels south of the 50°S latitude in in South Belet. One explanation as to the prevalence of channels in the South Belet high latitudes, compared to Afekan and Soi, is that more of the scalloped plains material has been eroded and removed via fluvial action, which would explain the patchiness of South Belet's scalloped plains. Other possibilities include less deposition in this area, thus allowing for more channels to remain unburied and exposed. Alternatively, it could be a difference in the material properties of the excavated substrate, or comparatively different trends in

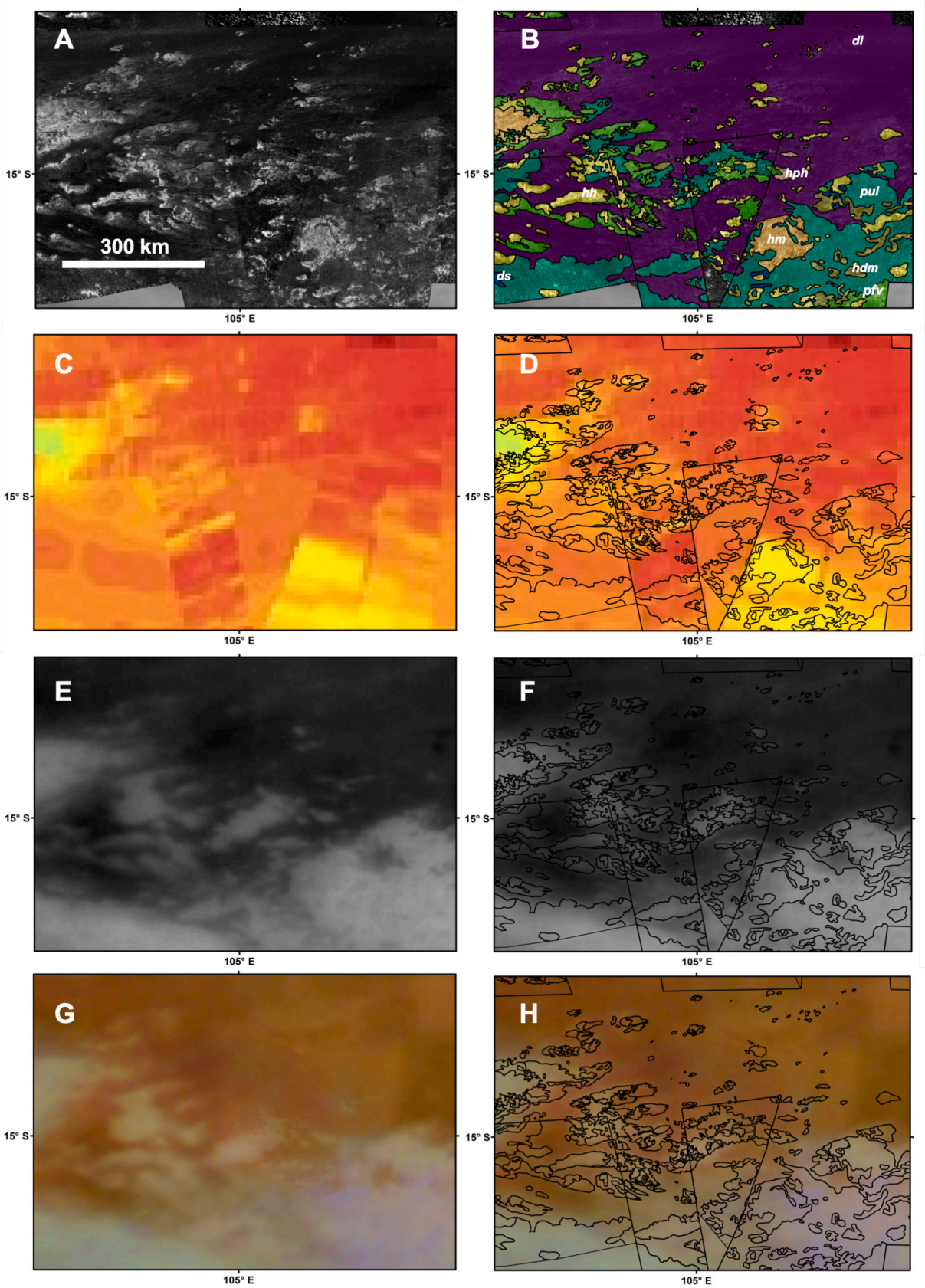

Fig. 13. Belet Sand Sea close-up (image centered at 13.7°S, 106.6°E): (A) SAR mosaic. (B) Annotated terrain map on the SAR mosaic. (C) Emissivity map. (D) Emissivity map showing contacts between terrain units. (E) ISS mosaic. (F) ISS mosaic showing contacts between terrain units. (G) VIMS RGB color ratio mosaic. (H) VIMS RGB color ratio mosaic showing contacts between terrain units.

precipitation.

The dark irregular plains are often found in contact with the scalloped plains. They are not extensive and occur only at higher mid-latitudes, but are found in Afekan, Soi, and South Belet. Like the scalloped plains, they appear around 50°S and extend toward the poles. The dark irregular plains correlate well with the low flat plains (Lf_d) unit from Birch et al. (2017). South Belet has comparatively more dark irregular plains than the other two regions, making up 1.3% of the mapped area in South Belet, 0.5% of the mapped area in Afekan, and 1% of the mapped area in Soi. We interpret this unit as composed of local basins that are dampened by liquid hydrocarbons either on the surface or within the top ~10's of centimeters of the surface (Janssen et al., 2016). However, the overall elevation with respect to the regional liquid table and surrounding terrains is unknown and may be variable. An alternative explanation is that this unit may contain finer grained materials than the surrounding terrain. They could also be small isolated areas of undifferentiated plains that have been identified as dark irregular terrains due to their smaller areal extent.

The 50° to 60° latitude zones, in both the northern and southern hemispheres, seem to represent a transitional region of sorts. The change in characteristic surface morphologies likely reflect a change from the aeolian dominated equatorial regions to the fluvially and lacustrine dominated poles.

5.2. The Belet Sand Sea

The majority of South Belet's linear dunes (*dl*) are located in the Belet Sand Sea (Fig. 13). Linear (or longitudinal) dunes appear as parallel, SAR-dark lines against a variable backscatter substrate and are similar in morphology to terrestrial dunes, such as Namibia, the Sahara, and Saudi Arabia (Lorenz et al., 2006; Neish et al., 2010; Radebaugh et al., 2010). The Belet Sand Sea consists of a wide belt of linear dunes with a sand transport direction inferred to be from west to east (Radebaugh et al., 2010; Malaska et al., 2016b).

Compared to other Titan sand seas, the dune forms in Belet are tightly spaced, straight, and very long (Radebaugh et al., 2008; Le Gall et al., 2012). Microwave emissivity data shows high emissivity for dune areas, but Belet is particularly emissive when compared to Titan's other dune fields, suggesting a low interdune to dune area ratio (Le Gall et al., 2012). The sum of these characteristics point to the Belet Sand Sea having a comparatively thick dune layer fed by a rich sand supply, perhaps with contributions from surface winds with particularly competent transport capacity (Kocurek and Lancaster, 1999). On Earth, dune fields commonly form within topographic basins where flow entering the basin expands, decelerates and results in the deposition of sediment (Wilson, 1971). Belet sits a few hundreds of meters below its surroundings, occupying a depression on Titan's trailing edge hemisphere (Stiles et al., 2009) that can readily concentrate windward materials.

Analysis by Bishop et al. (2017) found that dune widths in the Belet Sand Sea confirm a global correlation between decreasing dune width and increasingly northern latitudes (Le Gall et al., 2011, 2012). Additionally, they find that dune width and spacing correlate somewhat with longitude and decreases to the east. However, dune width and spacing typically increase in the migration direction, where dunes originate at the upwind margin of a field (Kocurek and Ewing, 2005), thus an opposite trend for dune width would be expected in a system where sand transport is from west to east, as is the case for Titan. It could be possible that the observed westward dipping regional slope is responsible for the field's observed spatial trends (Lorenz et al., 2013; Bishop et al., 2017; Telfer et al., 2019). However, latitudes roughly between 10°S and 20°S have been shown to be zones of sediment flux divergence (Lucas et al., 2014). This suggests that the transport is not solely eastward and thus could be affecting the width and spacing of the dunes. The observed dune patterns may be a result of the two factors combined.

5.3. Alluvial fans

In South Belet, areas of interpreted fluvial deposition are observed, but are not widespread (e.g. Fig. 8); these observations are similar to those made of the Afekan region and seem characteristic of Titan's mid-latitude and equatorial regions. However, SAR data were not able to resolve the networks visible in the Descent Imager / Spectral Radiometer (DISR) Huygens landing images (Jaumann et al., 2009), suggesting that the apparent scarcity of fluvial features in Cassini images should not be taken as evidence of their absence (Burr et al., 2013a). Channels that we do see are typically associated with the hummocky (*hh*) or mountain (*hm*) units. Such an association is well illustrated by an extensive system of channels found centered at 104.4°E, 28.29°S. While most of these channels terminate before the plains, some visibly extend from mountainous areas out onto the plains. The disappearance of channels into the plains could be due to several factors, including infiltration capacity of the undifferentiated plains, or also plain formation outpacing (burying or covering) channel incision (Lopes et al., 2016). Alternatively, the downstream portion of such channels may be less observable due to losses in contrast with their surroundings. The fact that some channels are seen within the undifferentiated plains unit suggests that these properties may be inhomogeneous within a given region.

In some instances, channels terminate into the *bright alluvial plains* (*pah*) unit (Fig. 10). Based on their triangular morphology and association with channel termini (Section 4.1), we interpreted this unit as alluvial fan-like deposits of high backscatter materials. Channels emerging from highland regions onto flat, low-lying plains deposit sediment into a cone-shaped fan, a consequence of the carrying capacity of the flow being suddenly reduced (Bull, 1977; Stock, 2013). Unlike fans on Earth and Mars, which are primarily composed of silicate rocks and transported by water, the mobilized materials on Titan's surface are most likely made of water ice and organics (Soderblom et al., 2007; Barnes et al., 2007a; Birch et al., 2016) and are transported by liquid hydrocarbon runoff (Lunine and Atreya, 2008; Birch et al., 2016). The similarity between Earth's and Titan's alluvial fans suggest similar underlying physical processes despite drastically different compositions of both fluids and sediments (Collins, 2005; Soderblom et al., 2007; Burr et al., 2013a; Birch et al., 2016).

We identify a total of three "bright alluvial plains" units in the South Belet region, all within the same ~28,000 km^2 region centered on 104.4°E, 28.29°S (Fig. 10b). SAR coverage in this area is limited, and thus the prevalence of alluvial fans in South Belet may be underestimated. Similarly, we are likely underestimating the number of fans in South Belet, and likely the whole moon, due to the coarse resolution of the Cassini SAR. Likewise, it is possible that any of the three fans identified here are actually a series of overlapping fans, or bajada-like structures, emanating from a single elevated region (Birch et al., 2016; Radebaugh et al., 2018). Regardless, no fans were identified within South Belet's well-imaged equatorial zone (<25°S) despite inferred observations of a large rainstorm at the equatorial regions (Turtle et al., 2011).

Birch et al. (2016) attributed the lack of fans in the equatorial regions to three factors. First, the landscape may have eroded to the point where sharp slope breaks are no longer available to generate fans at the observable resolution, despite a sufficiently energetic flow event. Second, precipitation at the equator may not be reaching headwater channels, instead infiltrating through a highly porous surface layer (Hayes et al., 2008; Birch et al., 2016). Third, equatorial fans are capable of forming at the observed scale but have subsequently been buried by aeolian sediments (Birch et al., 2016). Furthermore, Malaska et al. (2016a, 2016b) suggest that sediment transport in these areas is dominated by aeolian transport mechanisms, although some degree of recent equatorial fluvial activity is possible.

The global survey of Titan's alluvial fans presented in Birch et al. (2016) include the fans identified here. Their survey found that most fans are at latitudes between ±50–80°, with few observed fans seen

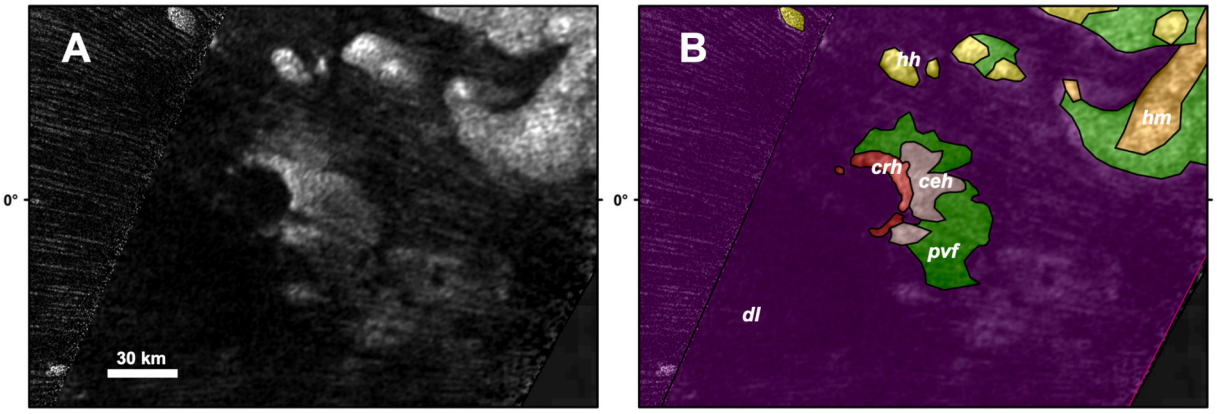

Fig. 14. Unnamed crater in South Belet (0.023°N, 79.51°W). (A) Unnamed crater in SAR. (B) Terrain unit mapping, including annotations of units.

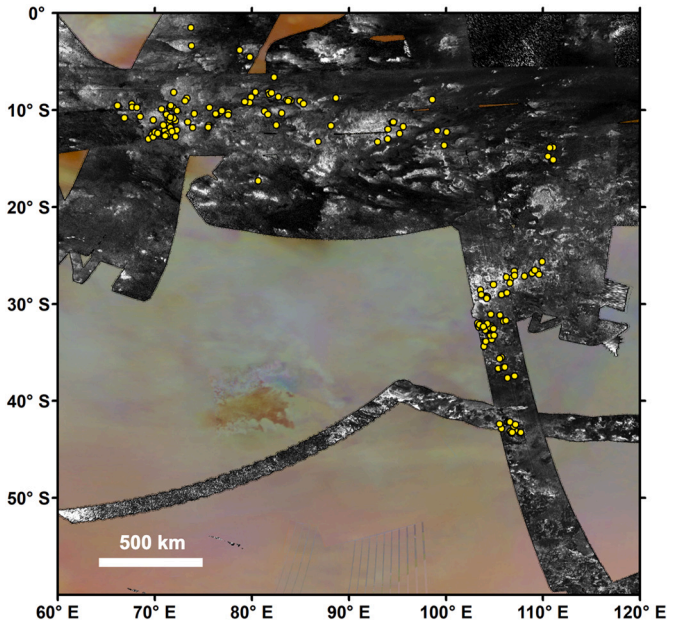

Fig. 15. SAR mosaic of the South Belet region. Location of individual pits marked in yellow. (For interpretation of the references to colour in this figure legend, the reader is referred to the web version of this article.)

within or in proximity to any of the equatorial dune fields. They also found a strong correlation between the latitudes of highest precipitation rates as predicted by Titan GCMs (e.g. Lora et al., 2014) and the latitudinal concentration of fans, suggesting a causal relationship. A study by Faulk et al. (2017) similarly found that storms capable of sediment transport and erosion occur at all latitudes in their simulations, consistent with the observed global coverage of fluvial features. However, the most extreme, high discharge storm events tend to occur in Titan's mid-latitudes, which are far more capable of transporting gravel-sized sediment than persistent low-magnitude precipitation. Consequently, such discharge events can leave geomorphic signatures in the form of large alluvial fans (e.g. Blair and McPherson, 2009; Leier et al., 2005; Borga et al., 2014). Furthermore, the Birch et al. (2016) study evaluates the fan area-drainage area relationships for Titan and finds that it supports a transport-limited sedimentary environment.

5.4. Impact processes

We have identified one (unnamed) crater in the South Belet region with confidence. The crater is ~26 km in diameter and is visible in HiSAR (Fig. 14).

Despite the lower resolution data, the morphology of this feature is semi-circular in nature, with a distinguishable rim and morphology similar to that of other Titan craters. The crater rim (*crh*) is seen to have been breached or overrun on the westward facing side, with linear dunes (*dl*) consequently invading the crater interior. There is a small zone of crater ejecta featured only on the eastward side of the rim, the rim presumably protecting the eastward ejecta from burial by the encroaching dunes. We interpret this crater as resulting from an impact into Titan's surface, bringing up deep crustal materials likely enriched in water ice. The crater rim was then eroded by aeolian and/or fluvial processes, creating a major breach on the western side of the rim and burying the western ejected deposits. Locations to the east of the crater were partially protected from dune transport and deposition, leaving a partially intact ejecta blanket. The breach of the rim is substantial, and thus the crater floor materials are likely aeolian materials transported from the west to the east. Other as-of-yet unidentified craters in the South Belet region have more than likely undergone a similar fate. Complete burial of craters, especially in and around the Belet Sand Sea, may explain the dramatic lack of craters in this region.

5.5. Equatorial pits in South Belet

Throughout South Belet, but specifically within the equatorial latitudes, there are numerous radar dark, circular features with diameters ranging in size from about 1–6 km. In total, 171 of these features were identified (Fig. 15). Similar features of this specific morphology, assumed to be depressions or pits, were first identified by Lopes et al. (2007) within Cassini's T8 swath. We primarily found these pits within a radar bright substrate resembling the "lumpy" internal texture of hummocky terrain; this association is the qualitative basis behind distinguishing "pitted hummocky" (*hpm*) from "hummocky" (*hh*). Pitted hummocky is also found in contact with mountainous (*hm*) and hummocky (*hh*) terrains (Fig. 11b). We interpret the radar-dark and smooth internal appearance of these features to be wind-blown organic sands deposited and concentrated into pre-existing depressions within exposure of the ancient ice crust.

The association between pits and Titan's mountainous units is compelling. It could be that, being locally elevated to the surrounding terrain, pitted depressions are preserved from complete burial by windward sediments and incidentally become associated with mountains and hummocks. Alternatively, the contrast in backscatter afforded by the radar bright substrate of the hummocky terrain makes the pits easier to identify; pits that may or may not be in the undifferentiated plains, for example, would be difficult to identify due to their comparable backscatters.

Based on morphological similarities, and their similar association with a radar-bright substrate, we interpret the pits found in South Belet

to have formed in the same manner as the pits found in the T8 SAR swath between 6°–12° south and 212°–230° west (Fig. 11f). As discussed in Lopes et al. (2007) and Lunine et al. (2008), the morphologies of these pits are not consistent with those of impact craters (e.g. Wood et al., 2010; Neish et al., 2013; Hedgepeth et al., 2020), lacking associated features such as a rim or ejecta blanket. Similarly, these pits have a modal diameter of 1–6 km, and do not have a size distribution consistent with impact craters. Regardless, any impactor that could be responsible for craters of this size would be too small (< 2 km) to pass through the atmosphere without breaking up (Lunine et al., 2005; Lunine et al., 2008). Secondary craters forming the pits is a possibility, but the distribution of the South Belet pits, very similar to the quasi-random distribution of pits within the mountain ranges of T8 (Adams and Jurdy, 2012), is not characteristic of chains of secondary craters. The general lack of a large primary impactor is likewise problematic. We hypothesize several alternative formation mechanisms and described them below.

5.5.1. Hypothesis #1: cryovolcanism

Cryovolcanism has been suggested as a method for pit formation on Titan by Lopes et al. (2007). Cryovolcanism is defined as eruptions of icy-cold aqueous solutions, or partly crystallized slurries, derived by partial melting of ice-bearing materials (Kargel, 1995). Lopes et al. (2007) suggests that the pits identified in the T8 SAR swath may be collapse or explosion pits, common in volcanic regions and thus may be related to cryovolcanism. While there is no morphological evidence of volcanic features such as flow fronts or calderas, in planform view the pits appearances are not unlike that of maar on Earth. Maar pits form via phreatomagmatic eruptions, or an explosion that is generated when ground water comes in contact with hot magma or lava, an example of which is Ubehebe Crater in Death Valley National Park, CA. A model for an analogous but Titan-appropriate process has been proposed by Mitri et al. (2019) and Wood and Radebaugh (2020) (see Section 5.6).

5.5.2. Hypothesis #2: "Sinkhole" formation via volatile loss

Pits observed on the Martian south polar cap have been attributed to sublimation (Thomas et al., 2000; Malin et al., 2001; Byrne and Ingersoll, 2003). In addition, pit formation on planetary surfaces is expected to form via collapse due to a cavity forming beneath the surface (Wyrick et al., 2004), such as through dissolution. Dissolution and/or sublimation processes requires an icy regolith that contains a sufficient fraction of volatile material to permit formation of pits several kilometers in size. However, water ice is both stable in Titan's atmosphere and insoluble in liquid methane/ethane (Lorenz and Lunine, 1996; Perron et al., 2006) and thus cannot be eroded by dissolution or sublimation. Small organic molecules such as acetylene, ethylene, propene, propyne (methylacetylene), cyclopropane, cyclopropene, all of which have been recently resolved in Titan's stratosphere (Thelen et al., 2019), are potentially volatile at Titan temperatures in the surface or near subsurface. However, these volatiles would likewise be soluble at the surface; relative rates of processing via either dissolution or sublimation of said volatiles have yet to be constrained.

If there were a volatile or semi-volatile substrate, however, then we can hypothesize that these pits formed via a type of sinkhole collapse, i.e. when the ceiling of a subsurface cavity can no longer support itself and fails, producing circular depressions aligned with the local gravity vector (Waltham et al., 2005). A potentially analogous process to the one proposed here is the outgassing of Mercury's volatile-rich (or at least historically volatile-rich) crust; on-going investigations indicate that Mercury's chaotic terrains and associated kilometer-scale "hollows" may have formed due to large-scale upper crustal devolatilization via various exogenic processes (Blewett et al., 2011; Blewett et al., 2013). Another analogous collapse mechanism to consider is pit formation on cometary nuclei, where removal of subsurface volatiles generates a void (Belton and Melosh, 2009; Vincent et al., 2015; Mousis et al., 2015). Failure of the cavity's ceiling propagates upward, resulting in quasi-circular depressions few tens to a few hundreds of meters in diameter, such as the pits observed by Rosetta on comet 67P (Vincent et al., 2015). Because the size of sinkholes depends on the material strength of the top layers, sinkholes in a given terrain are all of similar size (Waltham et al., 2005) and may explain the similarity in size of South Belet's pits, though it is possible that smaller pits exist beyond the scale of Cassini resolution.

5.5.3. Hypothesis #3: clathrate de-stabilization via tectonic shear heating

The presence of a large quantity of pits in proximity to the radar-bright mountains suggests the two may be related (Adams and Jurdy, 2012). Both extension fracturing and dilation faulting result in subsurface voids into which loose material on the surface can drain, creating linear assemblages of pits known as "pit chains" (Tanaka and Golombek, 1989; Ferrill et al., 2003; Wyrick et al., 2004; Martin et al., 2017). Radebaugh et al. (2007) describe the sub-parallel mountain ranges of T8 as possible extension features, although Liu et al. (2016a, 2016b) supersedes this idea and calls for contraction using methane ground fluids as lubricant. Adams and Jurdy (2012) explore an extensional origin for the T8 pits in more detail and finds statistical evidence of clustering throughout the entire pit field yet finds only a hint of linearity within those pit clusters when compared with a same-sized random set.

Whether from extensional or compressive tectonics, large scale mountain building in these areas will mechanically generate heat via the motion of faults, producing frictional heat from both shallow brittle deformation and deep plastic deformation in ductile shear zones (e.g. Scholz, 1980; Brewer, 1981). Transient shear heating during dynamic rupture of faults also can produce melting within a fault zone, given sufficiently large slip (e.g. McKenzie and Brune, 1972; Scholz, 1980; Lachenbruch, 1980). Methane stored as methane clathrates (Lunine and Stevenson, 1987) are highly stable in Titan's interior and thus their dissociation can occur only when the internal temperature reaches sufficiently high values (e.g. Grasset and Pargamin, 2005; Choukroun et al., 2010). It is worth considering the possibility that mechanical heating during a sufficiently large slip event (e.g. McKenzie and Brune, 1972) may facilitate the release of methane clathrates in the crust; gas generated in such an event may induce over-pressures required for creating cracks (Choukroun et al., 2010) that can be exploited and widened by erosion later.

5.5.4. Hypothesis 4: collapse via loss of fluid pressure

Pit collapse could be explained by the depletion of liquid methane in Titan's upper icy crust, which may lead to caprock collapse as a result of overburden pressures no longer being supported. Some sinkholes on Earth result from loss of buoyant support following a decline of the water table in the interior terrane, leading to the immediate collapse of the roofs of cavities in bedrock and unconsolidated deposits (e.g. Newton and Hyde, 1971; Spigner, 1978; Sinclair, 1982; Newton, 1987). The strong association between pits and mountainous terrains may be a factor, where highland topography is sufficiently removed from a receding ground-methane table, facilitating collapse. While the depth and extent of such a subsurface methane reservoir is unknown, liquid methane in Titan's crust is thought to have played an important role in mountain building on Titan (e.g. Liu et al., 2016b).

5.5.5. Hypothesis #5: formation via dissolution

Lastly, sinkhole-like collapse could be driven by dissolution of an organics/ice mixture. As previously discussed (Section 5.5.2.), the association of pits with the hummocky terrain suggests that they preferentially develop within an icy substrate. Water ice is insoluble in a landscape shaped by nonpolar solvents (Cornet et al., 2015), but this does not necessarily preclude the possibility of sinkhole collapse via dissolution. Though not constrained, a certain degree of mixing likely exists between the transition from surface organic regolith to buried icy crust, evoking the possibility of a heterogeneous media where dissolvable substrates can be dissolved in an otherwise insoluble matrix (e.g. Neish et al., 2015). Laboratory work has demonstrated dissolution of Titan's organic materials under cryogenic conditions (e.g. Malaska and

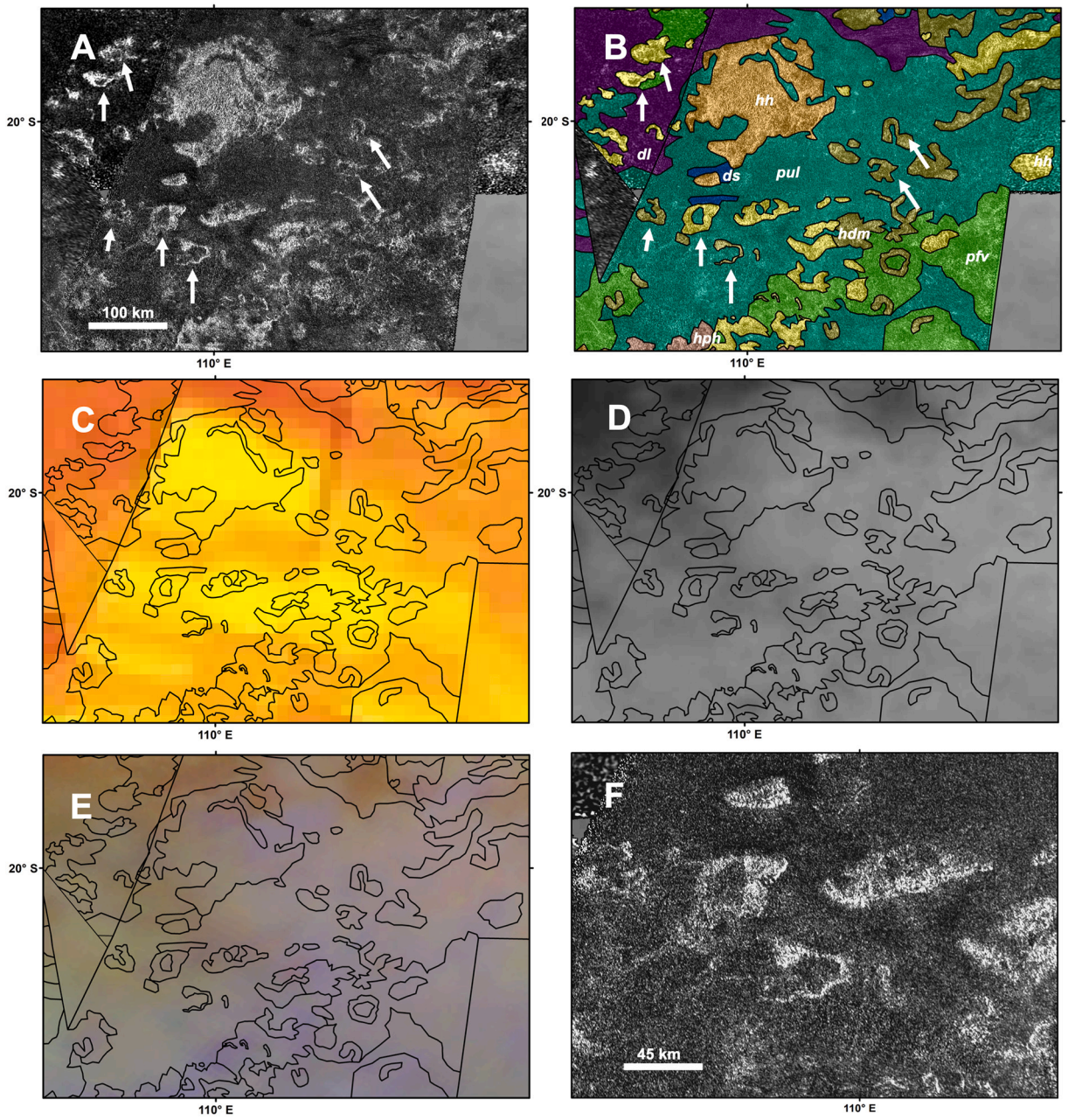

Fig. 16. Example area with "crescents". (A) SAR mosaic, crescents indicated with white arrows. (B) Terrain unit mapping, including annotations of units. White arrows indicate crescents. (C) Microwave emissivity map shown with contacts between terrain units. (D) ISS mosaic shown with contacts between terrain units. (E) VIMS RGB mosaic overlain with contacts between terrain units. (F) Zoom-in of several "crescents" that are indicated by the bottommost white arrows in (A).

Hodyss, 2014). Likewise, compelling geomorphologic interpretations exist for organic karstic processes on Titan, including evidence for karstic lakes, poljes, polygonal karst, fluviokarst, tower karst, and corrosion plains (Malaska et al., 2010, 2011, 2020; Cornet et al., 2015; Solomonidou et al., 2020b;). In addition, interpretations of evaporites (Barnes et al., 2011; MacKenzie et al., 2014), although not classically thought of as karstic landforms, provide observational evidence that dissolution and re-deposition has occurred on a large scale.

The pits seen in South Belet are larger than the largest sinkholes on Earth (~500 m; Waltham et al., 2005). Tectonic quiescence in more recent Titan epochs, as well as lower gravity, may allow Titan's voids to grow larger before finally collapsing (Mitchell and Malaska, 2011). In contrast, the largest pits observed on cometary nuclei such as 67P are an order of magnitude smaller (max ~300 m). This difference in size may be owing to a dramatic difference in strength of weakly bounded cometary materials (e.g. Groussin et al., 2019) when compared to ice at Titan conditions, despite a much smaller gravity field. Regardless, a more detailed analysis into the likelihood of sinkhole collapse on planetary bodies and the controls dominating size and distribution is warranted.

It is possible that the South Belet pits are more ubiquitous than suggested by the radar. For example, smaller, sub-resolution pits may be present yet remain unaccounted for. The pits identified, after all, are several kilometers in size, and possibly represent the extreme end member of the pit formation process, or the result of smaller pits coalescing into a larger one. It is also possible that the association between pit and hummocks are a result of locally high areas preferentially preserving the pits from complete burial by wind-ward sediments. Lastly, pits of similar morphological character are not restricted to the T8 swath nor South Belet and have been identified elsewhere in Titan's mid-

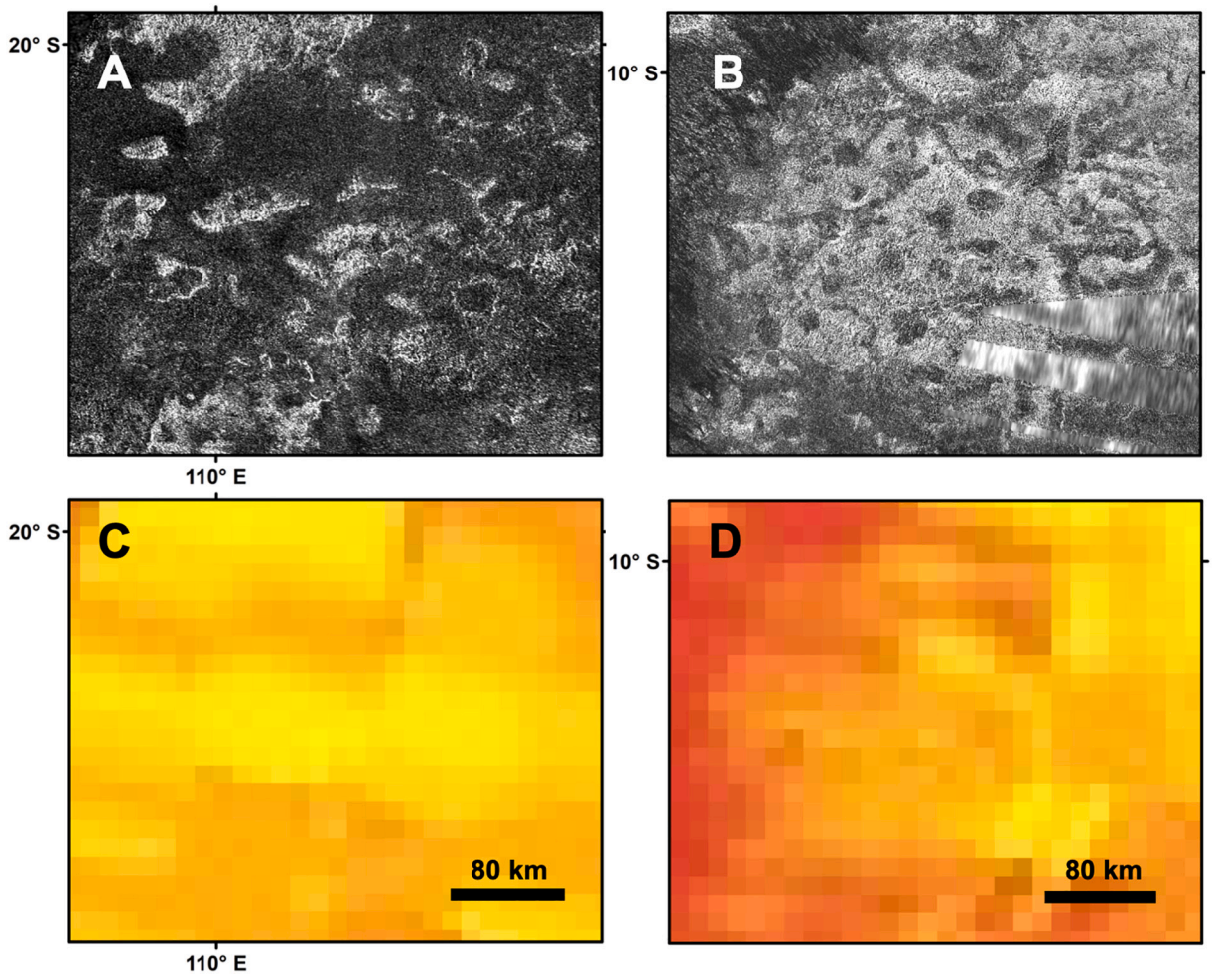

Fig. 17. (A) SAR mosaic of the "crescents" in South Belet. (B) SAR mosaic of western Xanadu. (C) Microwave emissivity map of the crescents in South Belet. (D) Microwave emissivity map of Western Xanadu.

latitudes. Titan's pits may represent a poorly understood erosional process with potential implications for methane replenishment of the atmosphere, as well as implications for sediment sources and sinks.

5.6. *"Crescents" of East South Belet*

East of the Belet Sand Sea are radar bright "crescent" features (Fig. 16) 15 to 35 km in diameter that have thus far not been described in the Titan literature. These features are also seen in other areas of Titan, including Afekan where they were mapped as "degraded hummocky terrain" (*hdm*). The number and spatial coverage of these features is extensive enough that the "crescent" may present a significant geologic process for Titan.

For the purposes of our mapping, we continue to label the crescents as "degraded hummocky" owing to their radar-bright appearance with a certain amount of dissection and burial. The degraded hummocky terrain (*hdm*) units are described in Malaska et al. (2016a) as small exposures of high-backscatter regions and are interpreted as remnants of hummocky terrain that have been eroded, and in some cases, partially buried by plains materials. What distinguishes the crescents from other "degraded hummocky" features are their irregular, pseudo-circular shape that partially encloses parts of the plains.

The irregular shape and rounded edges of the crescents are similar in morphology and size to many of the empty and filled sharp edged depressions (Hayes et al., 2017; Birch et al., 2018). Likewise, these crescents appear to have radar-bright "rims". These rims appear thicker in width than the raised rims (Birch et al., 2018) normally associated with the SEDs (~5 km here versus <1 km at the poles), but similar in thickness to the "ramparts" discussed in Solomonidou et al. (2020b) (which can be up to 10's of kms) and appear radar-bright and crenulated, closely resembling breached and partially eroded crater rims. Despite their crater-like appearance, their irregular shape presents a problem. Impact craters can lose their circular shape via tectonic processes, however there is not an obvious directional trend in deformation that could be associated with a regional process. In addition, the irregularity of the crescents does not resemble the tectonically deformed craters of other icy satellites (e.g. Pappalardo and Collins, 2005; Crow-Willard and Pappalardo, 2015; Kinczyk et al., 2019).

If not impact in origin, the crescent features may represent some evolutionary relationship between the pits described in the previous sections and the crescents discussed here. The crescents differ from the pits in that they are larger (15 to 35 km in diameter), more irregularly shaped, have a radar bright rim (though this may be a resolution effect), and in some cases are breached by plains material on one side. The crescents may represent the end stages of the pit formation process, a result of pits growing via lateral scarp retreat, ultimately coalescing together and creating irregular features. Alternatively, the crescent features may be analogous to that of explosion craters from magma–water interaction on Earth. Such a process has been proposed by Mitri et al. (2019) and Wood and Radebaugh (2020) to explain the formation of Titan's polar SEDs.

We make a final morphological comparison here in order to

understand the origin of the crescent features. It is possible that the crescents represent remnant exposures of a large icy substrate similar in morphology to northwestern Xanadu (Fig. 17) but that has been buried and breached by plains materials. The emissivity of this area is notably lower than the surrounding plains (Fig. 17c), suggesting near surface burial of a volume scattering material such as ice. The size and spacing of the crescents are also similar to that of the pseudo-circular depressions of Xanadu, which range in size from 7 to 27 km in diameter. Wall et al. (2009) and Nelson et al. (2009) proposed that the large depressions of western Xanadu are associated with cryovolcanic eruption and may be source vents, however other features related to volcanism such as flow fronts and depositions are lacking (Moore and Pappalardo, 2011). In a future study, it would be worthwhile to conduct a more detailed morphological analysis of Western Xanadu for comparison with the crescents in South Belet (and Afekan), as well as extend comparisons to other regions of cryovolcanic interest within Xanadu, such as Hotei and Tui Regio.

Regardless of origin, the preponderance of pseudo-circular features, whether as pits or crescents, on the surface of Titan suggest a complex erosional process that necessitates a more developed understanding of atmosphere/surface interactions, of the role of fluids in Titan's icy substrate and organic regolith, as well as of the role of endogenic activity in Titan's evolutionary history beyond mountain building.

5.7. Likely compositions

The surface diversity of Titan seen in ISS, VIMS, and RADAR observations provides evidence that Titan is not uniformly buried in organic dust (Barnes et al., 2007a), although the low contrast of surface images from the Huygens Landing Site analyzed in Karkoschka and Schröder (2016) indicate a uniform coating of materials. The likely surface composition of Titan's midlatitudes and equatorial regions are discussed in detail in Malaska et al. (2016a); based on the similarity of unit distribution and quantity, we suggest that the likely composition of South Belet is comparable to that of Afekan. For example, the radiometric and spectral signatures of the mountains, hummocky, and crater rim units are more consistent with materials containing water ice. Similarly, microwave emissivity data (Janssen et al., 2009, 2016; Malaska et al., 2020) and spectral analysis (Solomonidou et al., 2018) suggests that the dunes and plains, which make up the majority of Titan's surface materials, are consistent with organic materials.

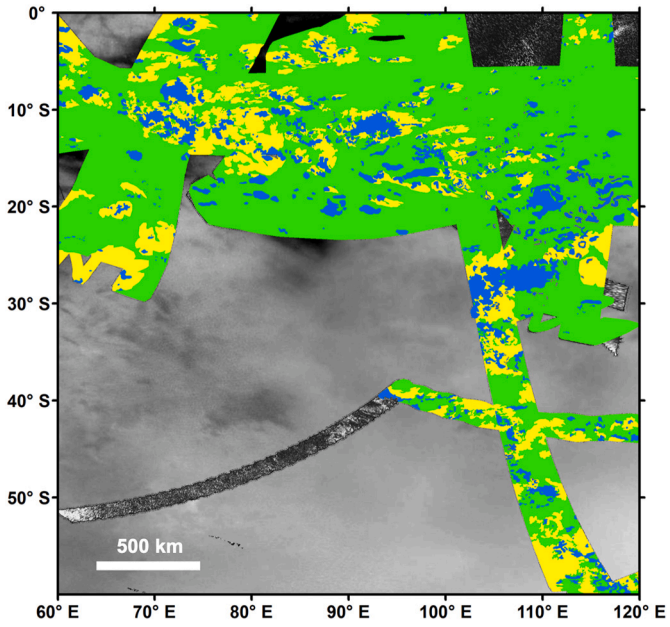

Fig. 18. Composition map of the South Belet region. Terrain types with properties consistent with organic materials are colorized in green, while those consistent with water ice are colorized in blue. Terrains of uncertain or mixed composition are colorized in yellow. (For interpretation of the references to colour in this figure legend, the reader is referred to the web version of this article.)

This picture is more complicated for the undifferentiated plains, where observations suggest latitudinal variations in composition within otherwise identical units. Using infrared surface reflectance with the Cassini VIMS instrument, Solomonidou et al. (2018) shows that plains closer to the equator have spectral similarities to that of the dunes, whereas water ice appears to be a major constituent of the plains beyond 30°N and 30°S. However, significant amounts of water ice are not expected to be present in these regions, given the lack of detection of high-dielectric constant material and high microwave emissivities (Janssen et al., 2016). Results from Solomonidou et al. (2020a) also show that craters in Titan's midlatitude plains are enriched in water ice in an organic based mixture, whereas equatorial dune craters appear to be purely composed of organic material. VIMS and radar probe different depths: a thin top layer in the case of VIMS, and a thicker layer in the case of radar. The existence of a thin layer of water ice (or of a material with a similar spectral response) covering organic material of low-dielectric constant is possible. Solomonidou et al. (2018) suggest that if this interpretation is correct, then more dark material is deposited from the atmosphere onto the equatorial regions compared to the higher latitudes and polar regions. Alternatively, atmospheric deposition is similar in the low and midlatitudes, but more rainfall may have been occurring for the higher latitudes causing additional modification of materials. The dark unknown material at higher latitudes could be either washed away or modified by rain so that it is no longer detectable.

Fig. 18 presents an inferred composition map of the South Belet region, similar to that presented in Malaska et al. (2016a, 2016b). Based on radiometric signatures and analyses of VIMS data (Jaumann et al., 2009; Lopes et al., 2016; Solomonidou et al., 2018), we determine that terrain units likely composed of organic materials include all dune units (*ds, dl*), the undifferentiated plains (*pul*), and the dark irregular plains (*pil*). Terrain units that are consistent with water ice materials (or other materials with similar emissivity and spectral properties) include the crater rim (*crh*), crater ejecta (*ceh*), mountain (*hm*), hummocky (*hh*), degraded hummocky (*hdm*), the pitted hummocky (*hph*) terrain units, and the bright alluvial plains (*pah*). Terrain units that are of indeterminate composition or may represent a mix of water ice and organic materials include the variable plains terrains (*pfv*, which by definition, are variable in composition) and scalloped plains (*psv*). The area percentages for South Belet show that the likely organic-rich terrains make up over 71.8% of Titan's surface in this area. Areas that are consistent with being rich in water–ice materials make up 10.6% of South Belet's surface, suggesting that, at least by areal coverage, Titan's uppermost surface is primarily composed of organic materials, a result similarly found for Afekan.

6. Geologic history

We update the relative stratigraphic relations established in Malaska et al. (2016a) for the South Belet region and graphically show their correlation in Fig. 19. Relative superposition of terrain units were used to determine a relative sequence in Afekan and now in South Belet. Topographic data, where available, was used to confirm relations between terrain units. See Malaska et al. (2016a) for a more detailed discussion.

Following previous interpretations, South Belet's geologic history presents a story familiar to that of Afekan, but with some notable differences. The hummocky (*hh*) and mountainous terrain (*hm*) of South Belet are likely remnant exposures of Titan's ancient icy crust. The crust may originally have been impact-scarred, but subsequent erosion and depositional processes have erased any record of these impacts. Pits within the icy crust, constituting the pitted hummocky terrain (*hph*),

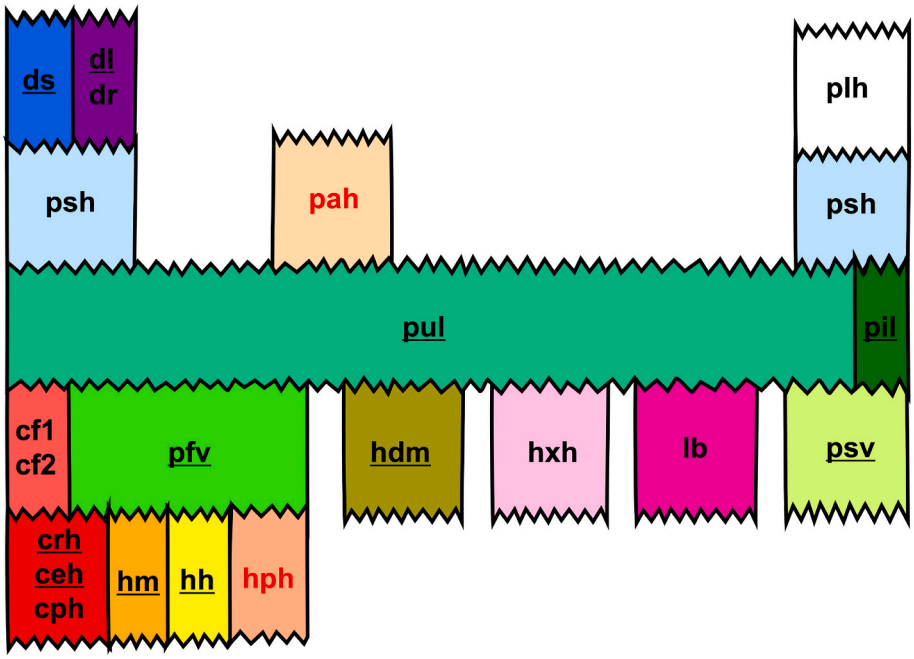

Fig. 19. Relative stratigraphy of terrain units from Afekan and South Belet. Red text indicates new units introduced in this paper, whereas underlined units indicate units that appear both in Afekan and South Belet. Units adjacent in the graphics represent direct contact seen in SAR. Units that do not touch in the graphic represent where superposition could not be determined from the SAR. The main units used to determine relative stratigraphy is the undifferentiated plains (*pul)*. Units are: *crh* = crater rim, *ceh* = crater ejecta, *cph* = central peak, *cf1* = crater fill 1, *cf2* = crater fill 2, *hm* = mountain, *hh* = hummocky, *hph* = pitted hummocky, *hdm* = degraded hummocky, *hxh* = cross-cut hummocky, *lb* = labyrinth, *pah* = bright alluvial plains, *pil* = dark irregular plains, *pfv* = variable featured plains, *pul* = undifferentiated plains, *psv* = scalloped plains, *psh* = streak-like plains, *plh* = lineated plains, *dl* = linear dunes, *ds* = featureless sand sheets, *dr* = reticulated dunes. (For interpretation of the references to colour in this figure legend, the reader is referred to the web version of this article.)

may have formed via dissolution or sublimation processes, or may have some connections to Titan's tectonic past. The linear orientation of some of Titan's mountains suggest some underlying tectonic fabric, whether from extension or compression, led to their uplift (Mitri et al., 2010; Cook-Hallett et al., 2015; Liu et al., 2016a, 2016b). Plains and dune materials have more recently been deposited onto, and subsequently buried, the eroded landscape, partially filling or embaying craters and pits alike (e.g. Werynski et al., 2019).

Studies of surface material transport directions (Malaska et al., 2016b) and analysis of spectral data from VIMS (Lopes et al., 2016; Solomonidou et al., 2018) suggest that the materials from the dune terrains (*ds* and *dl*) eventually evolve into the materials making up the mid-latitude undifferentiated plains (*pul*; Lopes et al., 2016; Malaska et al., 2016b; Solomonidou et al., 2018). Solomonidou et al. (2018) show that the undifferentiated plains have a much stronger 2-μm absorption than the dunes, suggesting there is a constituent in the mix that ultimately plays a role in differentiating the two units.

In the equatorial regions and mid-latitudes, materials eroded from the mountains likely mix with adjacent organic materials, eventually resulting in the variable featured plains (*pfv*). This is consistent with results from VIMS that show that the surface albedo values of variable plains are intermediate between equatorial undifferentiated plains and dunes, as if some process mixed the two (Solomonidou et al., 2018). In the equatorial region, the dunes eventually bury these deposits as they migrate in a predominantly west to east direction. In the mid-latitudes, sediments derived from erosion of the mountains are embayed by windward undifferentiated plains (Lopes et al., 2016). Otherwise, fluvial channels may have abraded and transported material from the mountains, delivering sediment and depositing it as the fan-shaped bright alluvial plains (*pah*).

7. Summary

Here we have presented and described a geomorphologic map of the South Belet region of Titan. We used Cassini SAR as our basemap, supplemented with other datasets such as radiometry, topography, ISS, and VIMS. This entire region makes up 11.3% of Titan's areal surface, whereas the parts of the region imaged by SAR make up 3.6% of Titan's surface. This area represents the main geological processes that have occurred in Titan's equatorial and the southern mid-latitudes. We identified and described two new terrain units, the "bright alluvial plains" and the "pitted hummocky", adding to the mapping units discussed in Malaska et al. (2016a). Following previous interpretations, South Belet's geologic history presents a story familiar to that of Afekan, but with some notable differences. Similar to the Afekan region, there are four major classes of terrain units in South Belet: dunes, plains, mountain/hummocky, and crater. Noticeably missing from South Belet is the fifth and sixth major class of unit, the labyrinths and the basin and lake units. We find that plains dominate the make-up of this region, accounting for 47.0% of the mapped area, followed by dunes (43.0%), mountains/hummocky terrains (11.0%), and crater terrains (<<1%). The emissivity and spectral properties of the undifferentiated plains and dunes have emissivity and spectral properties consistent with organic materials, whereas the emissivity and spectral properties of the mountain/hummocky and crater terrains are more consistent with water ice. Only one crater has been identified in South Belet with confidence, which may be a consequence of both spatial coverage bias (especially in areas away from dunes) and burial capacity of the Belet Sand Sea.

We only observe small instances of fluvial transport in South Belet, such as the alluvial plains. Instead, material transport patterns are more consistent with widespread aeolian deposition of dunes and plains units. If fluvial activity was once more present in this region, it has since been buried by aeolian deposits. We identified three "bright alluvial plains" that we interpret to be alluvial fans. Fans, like the equatorial dunes, are part of a limited set of depositional features identified on Titan. Likely alluvial in origin (e.g. Birch et al., 2016), the identification of fans on Titan's surface indicate that discharges and slopes are such that sediment can be mobilized and ultimately deposited. We additionally introduce another unit not previously discussed in Malaska et al., (2016a): pitted hummocky (*hph*). We interpret this unit to be an icy substrate with 1–6 km sized "pits" and hypothesize that these pits may have formed as a result of either cryovolcanism, the removal of methane (either from outgassing or the retreat of a ground reservoir) in the near surface, or as a result of the dissolution of soluble organics in an otherwise icy matrix. Given our proposed origins, pit formation was either coeval with the uplift of Titan's mountains or formed subsequently via atmospheric or ground fluid interactions with Titan's near subsurface. Eventually, the pits were infilled with windward dune material. The introduction of these two new units are necessary to capture the full range of morphologies seen in South Belet, and likewise indicate

a morphological departure from Afekan. We also discussed Titan's "crescents", radar bright features 15 to 35 km in diameter that have thus far not been described in the Titan literature. We find that the crescents are morphologically similar to polar "sharp-edged depressions" (SEDs) as well as to the icy exposures of northwestern Xanadu. We propose that these pseudo-circular features may represent the end-stage evolution of the aforementioned pits or are perhaps relics of past cryovolcanism.

Our geomorphological mapping results for South Belet is consistent with the narrative of Titan's equatorial and mid-latitudes being dominated by organic materials that have been deposited and emplaced by aeolian activity. This is likewise the conclusion we arrived at through our mapping and analysis of the Afekan region. Additionally, the presence of similar units found in both Afekan and South Belet suggests latitudinal symmetry in Titan's surface processes and their evolution.

Declaration of Competing Interest

None

Acknowledgements

We wish to thank the entire Cassini RADAR Team and the Cassini mission scientists and engineers for their hard work that made this exploration possible. AMS is supported by an NSF graduate student fellowship, grant number DGE-1650604. Parts of this work were funded by two Cassini Data Analysis grants to R. Lopes (NNN13D466T and NH16ZDA001N). AS was partially supported by the Czech Science Foundation (grant number 20-27624Y). DAW is supported by grant number NNX14AR29G from NASA's Outer Planets Research Program. This work was carried out at the Jet Propulsion Laboratory, California Institute of Technology, under contract with NASA. Copyright 2020, California Institute of Technology. Government sponsorship is acknowledged.

References

Adams, K.A., Jurdy, D.M., 2012. Pit distribution in the equatorial region of Titan. Planet. Space Sci. 65, 58–66.

Atreya, S.K., Adams, E.Y., Niemann, H.B., Demick-Montelara, J.E., Owen, T.C., Fulchignoni, M., Ferri, F., Wilson, E.H., 2006. Titan's methane cycle. Planet. Space Sci. 54, 1177–1187.

Barnes, J.W., Brown, R.H., Soderblom, L., Buratti, B.J., Sotin, C., Rodriguez, S., Le Mouèlic, S., Baines, K.H., Clark, R., Nicholson, P., 2007a. Global-scale surface spectral variations on Titan seen from Cassini/VIMS. Icarus 242, 258. https://doi.org/10.1016/j.icarus.2006.08.021.

Barnes, J.W., Radebaugh, J., Brown, R.H., Wall, S., Soderblom, L., Lunine, J., Burr, D., Sotin, C., Le Mouélic, S., Rodriguez, S., Buratti, B.J., Clark, R., Baines, K.H., Jaumann, R., Nicholson, P.D., Kirk, R.L., Lopes, R., Lorenz, R.D., Mitchell, K., Wood, C.A., 2007b. Near-infrared spectral mapping of Titan's mountains and channels. J. Geophys. Res. 112, E11006 https://doi.org/10.1029/2007JE002932.

Barnes, J.W., Bow, J., Schwartz, J., Brown, R.H., Soderblom, J.M., Hayes, A.G., Vixie, G., Le Mouélic, S., Rodriguez, S., Sotin, C., Jaumann, R., 2011. Organic sedimentary deposits in Titan's dry lakebeds: Probable evaporite. Icarus 216, 136–140.

Barnes, J.W., Lorenz, R.D., Radebaugh, J., Hayes, A.G., Arnold, K., Chandler, C., 2015. Production and global transport of Titan's sand particles. Planet. Sci. 4, 1–19.

Belton, M.J., Melosh, J., 2009. Fluidization and multiphase transport of particulate cometary material as an explanation of the smooth terrains and repetitive outbursts on 9P/Tempel 1. Icarus 200, 280–291.

Birch, S.P.D., Hayes, A.G., Howard, A.D., Moore, J.M., Radebaugh, J., 2016. Alluvial fan morphology, distribution and formation on Titan. Icarus 270, 238–247. https://doi.org/10.1016/j.icarus.2016.02.013.

Birch, S.P.D., Hayes, A.G., Dietrich, W.E., Howard, A.D., Bristow, C.S., Malaska, M.J., Moore, J.M., Mastroguiseppe, M., Hofgartner, J.D., Williams, D.A., White, O.L., Soderblom, J.M., Barnes, J.W., Turtle, E.P., Lunine, J.I., Wood, C.A., Neish, C.D., Kirk, R.L., Stofan, E.R., Lorenz, R.D., Lopes, R.M.C., 2017. Geomorphologic mapping of Titan's polar terrains: constraining surface processes and landscape evolution. Icarus 282, 214–236. https://doi.org/10.1016/j.icarus.2016.08.003.

Birch, S.P.D., Hayes, A.G., Corlies, P., Stofan, E.R., Hofgartner, J.D., Lopes, R.M.C., Lorenz, R.D., Lunine, J.I., MacKenzie, S.M., Malaska, M.J., Wood, C.A., 2018. Morphological evidence that Titan's southern hemisphere basins are paleoseas. Icarus 310, 140–148.

Bishop, B., Lewis, R.C., Radebaugh, J., Christiansen, E.H., 2017. Spatial variations of dune parameters and relationship to elevation and geographic position within the Belet sand sea. LPI 1964, 2425.

Blair, T.C., McPherson, J.G., 2009. Processes and forms of alluvial fans. In: Abrahams, A. D., Parsons, A.J. (Eds.), Geomorphology of Desert Environments, 2nd ed. Chapman & Hall, pp. 454–456.

Blewett, D.T., Chabot, N.L., Denevi, B.W., Ernst, C.M., Head, J.W., Izenberg, N.R., Murchie, S.L., Solomon, S.C., Nittler, L.R., McCoy, T.J., Xiao, Z., 2011. Hollows on Mercury: MESSENGER evidence for geologically recent volatile-related activity. Science 333, 1856–1859.

Blewett, D.T., Vaughan, W.M., Xiao, Z., Chabot, N.L., Denevi, B.W., Ernst, C.M., Helbert, J., D'Amore, M., Maturilli, A., Head, J.W., Solomon, S.C., 2013. Mercury's hollows: constraints on formation and composition from analysis of geological setting and spectral reflectance. J. Geophys. Res. Planet 118, 1013–1032.

Borga, M., Stoffel, M., Marchi, L., Marra, F., Jakob, M., 2014. Hydrogeomorphic response to extreme rainfall in headwater systems: flash floods and debris flows. J. Hydrol. 518, 194–205.

Brewer, J., 1981. Thermal effects of thrust faulting. Earth Planet. Sci. Lett. 56, 233–244.

Brossier, J.F., Rodriguez, S., Cornet, T., Lucas, A., Radebaugh, J., Maltagliati, L., Le Mouélic, S., Solomonidou, A., Coustenis, A., Hirtzig, M., Jaumann, R., 2018. Geological evolution of Titan's equatorial regions: possible nature and origin of the dune material. J. Geophys. Res. Planet 123 (5), 1089–1112.

Brown, R.H., Baines, K.H., Bellucci, G., Bibring, J.-B., Buratti, B.J., Capaccioni, F., Cerroni, P., Clark, R.N., Coradini, A., Cruikshank, D.P., Drossart, P., Formisano, V., Jaumann, R., Langevin, Y., Matson, D.L., McCord, T.B., Mennella, V., Miller, E., Nelson, R.M., Nicholson, P.D., Sicardy, B., Sotin, C., 2004. The Cassini Visual and Infrared Mapping Spectrometery (VIMS) investigation. Space Sci. Rev. 115, 111–168. https://doi.org/10.1007/s11214-004-1453-x.

Brown, R.H., Soderblom, L.A., Soderblom, J.M., Clark, R.N., Jaumann, R., Barnes, J.W., Sotin, C., Buratti, B., Baines, K.H., Nicholson, P.D., 2008. The identification of liquid ethane in Titan's Ontario Lacus. Nature 454, 607–610.

Bull, W.B., 1977. The alluvial-fan environment. Prog. Phys. Geogr. 1, 222–270.

Burr, D.M., Jacobsen, R.E., Roth, D.L., Phillips, C.B., Mitchell, K.L., Viola, D., 2009. Fluvial network analysis on Titan: evidence for subsurface structures and west to east wind flow, southwestern Xanadu. Geophys. Res. Lett. 36, L22203 https://doi.org/10.1029/2009GL040909.

Burr, D.M., Perron, J.T., Lamb, M.P., Iriwin III, R.P., Collins, G.C., Howard, A.D., Sklar, L. S., Moore, J.M., Ádámkovics, M., Baker, V.R., Drummond, S.A., Black, B.A., 2013a. Fluvial features on Titan: insights from morphology and modeling. Geol. Soc. Am. Bull. 125, 299–321. https://doi.org/10.1130/B30612.1.

Burr, D.M., Drummond, S.A., Cartwright, R., Black, B.A., Perron, J.T., 2013b. Morphology of fluvial networks on Titan: evidence for structural control. Icarus 226 (1), 742–759.

Byrne, S., Ingersoll, A.P., 2003. A sublimation model for Martian south polar ice features. Science 299, 1051–1053.

Choukroun, M., Grasset, O., Tobie, G., Sotin, C., 2010. Stability of methane clathrate hydrates under pressure: influence on outgassing processes of methane on Titan. Icarus 205, 581–593.

Clark, R.N., Curchin, J.M., Barnes, J.W., Jaumann, R., Soderblom, L., Cruikshank, D.P., Brown, R.H., Rodriguez, S., Lunine, J., Stephan, K., Hoefen, T.M., Le Mouelic, S., Sotin, C., Baines, K.H., Buratti, B.J., Nicholson, P.D., 2010. Detection and mapping of hydrocarbon deposits on Titan. J. Geophys. Res. 115, E10005 https://doi.org/10.1029/2009JE003369.

Collins, G.C., 2005. Relative rates of fluvial bedrock incision on Titan and Earth. Geophys. Res. Lett. 32, L22202.

Cook-Hallett, C., Barnes, J.W., Kattenhorn, S.A., Hurford, T., Radebaugh, J., Stiles, B., Beuthe, M., 2015. Global contraction/expansion and polar lithospheric thinning on Titan from patterns of tectonism. J. Geophys. Res. Planet 120, 1220–1236. https://doi.org/10.1002/2014JE004645.

Corlies, P., Hayes, A.G., Birch, S.P.D., Lorenze, R., Stiles, B.W., Kirk, R., Poggiali, V., Zebker, H., Iess, L., 2017. Titan's topography and shape at the end of the Cassini mission. Geophys. Res. Lett. 44, 11754–11761. https://doi.org/10.1002/2017GL075518.

Cornet, T., Cordier, D., Bahers, T.L., Bourgeois, O., Fleurant, C., Mouélic, S.L., Altobelli, N., 2015. Dissolution on Titan and on Earth: toward the age of Titan's karstic landscapes. J. Geophys. Res. Planet 120, 1044–1074.

Crow-Willard, E.N., Pappalardo, R.T., 2015. Structural mapping of Enceladus and implications for formation of tectonized regions. J. Geophys. Res. Planet 120, 928–950.

Elachi, C., Allison, M., Anderson, Y., Boehmer, R., Callahan, P., Encrenaz, P., Flameni, E., Francescetti, G., Gim, Y., Hamilton, G., Hensley, S., Janssen, M., Johnson, W., Kelleher, K., Kirk, R., Lopes, R., Lorenz, R., Lunine, J., Muhleman, D., Ostro, S., Paganelli, F., Picardi, G., Posa, F., Roth, L., Seu, R., Shaffer, S., Soderblom, L., Stiles, B., Stofan, E., Vetrella, S., Wall, S., West, R., Wood, C., Wye, L., Zebker, H., 2005a. Cassini RADAR's first view of the surface of Titan. Science 13, 970–974.

Elachi, C., Allison, M.D., Borgarelli, L., Encrenaz, P., Im, E., Janssen, M.A., Johnson, W.T. K., Kirk, R.L., Lorenz, R.D., Lunine, J.I., Muhleman, D.O., Ostro, S.J., Picardi, G., Posa, F., Rapley, C.G., Roth, L.E., Seu, R., Soderblom, L.A., Vetrella, S., Wall, S.D., Wood, C.A., Zebker, H.A., 2005b. RADAR: the Cassini Titan radar mapper. Space Sci. Rev. 117, 71–110.

Elachi, C., Wall, S., Janssen, M., Stofan, E., Lopes, R., Kirk, R., Lorenz, R., Lunine, J., Paganelli, F., Soderblom, L., Wood, C., Wye, L., Zebker, H., Anderson, Y., Ostro, S., Allison, M., Boehmer, R., Callahan, P., Encrenaz, P., Flamini, E., Francescetti, G., Gim, Y., Hamilton, G., Hensley, S., Johnson, W., Kelleher, K., Muhleman, D., Picardi, G., Posa, F., Roth, L., Seu, R., Shaffer, S., Stiles, B., Vetrella, S., West, R., 2006. Titan radar mapper observations from Cassini's T3 fly-by. Nature 441, 709–713. https://doi.org/10.1038/nature04786.

Faulk, S.P., Mitchell, J.L., Moon, S., Lora, J.M., 2017. Regional patterns of extreme precipitation on Titan consistent with observed alluvial fan distribution. Nat. Geosci. 10, 827–831.
Ferrill, D.A., Morris, A.P., Waiting, D.J., Franklin, N.M., Sims, D.W., 2003. Influence of gravity on the geometry of Martian normal faults. In: Lunar and Planetary Science Conference, vol. 34. March.
Fulchignoni, M., Ferri, F., Angrilli, F., Ball, A.J., Bar-Nun, A., Barucci, M.A., Bettanini, C., Bianchini, G., Borucki, W., Colombatti, G., Coradini, M., Coustenis, A., Debei, S., Falkner, P., Fanti, G., Flamini, E., Gaborit, V., Grard, R., Hamelin, M., Harri, A.M., Hathi, B., Jernej, I., Leese, M.R., Lehto, A., Lion Stoppato, P.F., López-Moreno, J.J., Mäkinen, T., McDonnell, J.A.M., McKay, C.P., Molina-Cuberos, G., Neubauer, F.M., Pirronello, V., Rodrigo, R., Saggin, B., Schwingenschuh, K., Seiff, A., Simões, F., Svedhem, H., Tokano, T., Towner, M.C., Trautner, R., Withers, P., Zarnecki, J.C., 2005. In situ measurements of the physical characteristics of Titan's environment. Nature 438, 785–791. https://doi.org/10.1038/nature04314.
Grasset, O., Pargamin, J., 2005. The ammonia–water system at high pressures: implications for the methane of Titan. Planet. Space Sci. 53, 371–384.
Greeley, R., Batson, R.M., 1990. Planetary Mapping. Cambridge University Press, New York.
Griffith, C.A., Penteado, P.F., Turner, J.D., Neish, C.D., Mitri, G., Montiel, N.J., Schoenfeld, A., Lopes, R.M., 2019. A corridor of exposed ice-rich bedrock across Titan's tropical region. Nat. Astr. 3, 642–648.
Groussin, O., Attree, N., Brouet, Y., Ciarletti, V., Davidsson, B., Filacchione, G., Fischer, H.H., Gundlach, B., Knapmeyer, M., Knollenberg, J., Kokotanekova, R., 2019. The thermal, mechanical, structural, and dielectric properties of cometary nuclei after Rosetta. Space Sci. Rev. 215, 29.
Hayes, A., Aharonson, O., Callahan, P., Elachi, C., Gim, Y., Kirk, R., Lewis, K., Lopes, R., Lorenz, R., Lunine, J., Mitchell, K., Mitri, G., Stofan, E., Wall, S., 2008. Hydrocarbon lakes on Titan: distribution and interaction with a porous regolith. Geophys. Res. Lett. 35, L09204 https://doi.org/10.1029/2008GL033409.
Hayes, A.G., Birch, S.P.D., Dietrich, W.E., Howard, A.D., Kirk, R.L., Poggiali, V., Mastrogiuseppe, M., Michaelides, R.J., Corlies, P.M., Moore, J.M., Malaska, M.J., 2017. Topographic constraints on the evolution and connectivity of Titan's lacustrine basins. Geophys. Res. Lett. 44, 11–745.
Hayes, A.G., Lorenz, R.D., Lunine, J.I., 2018. A post-Cassini view of Titan's methane-based hydrologic cycle. Nat. Geosci. 11, 306–313. https://doi.org/10.1038/s41561-018-0103-y.
Hedgepeth, J.E., Neish, C.D., Turtle, E.P., Stiles, B.W., Kirk, R., Lorenz, R.D., 2020. Titan's impact crater population after Cassini. Icarus 113664.
Janssen, M.A., Lorenz, R.D., West, R., Paganelli, F., Lopes, R.M., Kirk, R.L., Elachi, C., Wall, S.D., Johnson, W.T.K., Anderson, Y., Boehmer, R.A., Callahan, P., Gim, Y., Hamilton, G.A., Kelleher, K.D., Roth, L., Stiles, B., Le Gall, A., Cassini RADAR Team, 2009. Titan's Surface at 2.2-cm wavelength imaged by the Cassini RDAR radiometer: calibration and first results. Icarus 200, 222–239. https://doi.org/10.1016/j.icarus.2008.10.017.
Janssen, M.A., Le Gall, A., Wye, L.C., 2011. Anomalous radar backscatter from Titan's surface? Icarus 212, 321–328.
Janssen, M.A., Le Gall, A., Malaska, M.J., Lopes, R.M., Lorenz, R.D., Malaska, M.J., Hayes, A.G., Neish, C.D., Solomonidou, A., Mitchell, K.L., Radebaugh, J., Keihm, S.J., Choukroun, M., Leyrat, C., Encrenaz, P.J., Mastroguiseppe, M., 2016. Titan's surface at 2.218-cm wavelength wavelength imaged by the Cassini RADAR radiometer: results and interpretation through the first ten years of observations. Icarus 270, 443–459. https://doi.org/10.1016/j.icarus.2015.09.027.
Jaumann, R., Brown, R.H., Stephan, K., Barnes, J.W., Soderblom, L.A., Sotin, C., Le Mouélic, S., Clark, R.N., Soderblom, J., Buratti, B.J., Wagner, R., McCord, T.B., Rodriguez, S., Baines, K.H., Cruikshank, D.P., Nicholson, P.D., Griffith, C.A., Langhans, M., Lorenz, R.D., 2008. Fluvial erosion and post-erosional processes on Titan. Icarus 197, 526–538. https://doi.org/10.1016/j.icarus.2008.06.002.
Jaumann, R., Kirk, R.L., Lorenz, R.D., Lopes, R.M.C., Stofan, E., Turtle, E., Keller, P., Wood, H.U., Sotin, C.A., Soderblom, C., Tomasko, L.A., 2009. Geology and surface processes on Titan. In: Brown, R.H., Leberton, J.-P., Waite, J.H. (Eds.), Titan from Cassini-Huygens. Springer, New York, pp. 75–140.
Jennings, D.E., Cottini, V., Nixon, C.A., Achterberg, R.K., Flasar, F.M., Kunde, V.G., Romani, P.N., Samuelson, R.E., Mamoutkine, A., Gorius, N.J.P., Coustenis, A., Tokano, T., 2016. Surface temperatures on Titan during northern winter and spring. AstroPhys. J. Lett. 816, L17. https://doi.org/10.3847/2041-8205/816/1/L17.
Kargel, J.S., 1995. Cryovolcanism on the icy satellites. In: Comparative Planetology with an Earth Perspective. Springer, Dordrecht, pp. 101–113.
Karkoschka, E., Schröder, S.E., 2016. Eight-color maps of Titan's surface from spectroscopy with Huygens' DISR. Icarus 270, 260–271.
Karkoschka, E., McEwen, A., Perry, J., 2017. Producing the Best Global Mosaic of Titan's Surface Albedo Using Cassini Images. LPSC 48, #2518.
Kinczyk, M.J., Byrne, P.K., Collins, G.C., Patterson, G.W., Bohnenstiehl, D.R., 2019. Stress risers in Enceladus' cratered terrain. LPI 2132, 1446.
Kirk, R.L., Callahan, P., Seu, R., Lorenz, R.D., Paganelli, F., Lopes, R., Elachi, C., 2005. RADAR Reveals Titan Topography.
Kocurek, G., Ewing, R.C., 2005. Aeolian dune field self-organization–implications for the formation of simple versus complex dune-field patterns. Geomorphology 72, 94–105.
Kocurek, G., Lancaster, N., 1999. Aeolian system sediment state: theory and Mojave Desert Kelso dune field example. Sedimentology 46, 505–515.
Krasnopolsky, V.A., 2009. A photochemical model of Titan's atmosphere and ionosphere. Icarus 201, 226–256. https://doi.org/10.1016/j.icarus.2008.12.038.
Krasnopolsky, V., 2014. Chemical composition of Titan's atmosphere and ionosphere: observations and the photochemical model. Icarus 236 (2014), 83–91. https://doi.org/10.1016/j.icarus.2014.03.041.
Lachenbruch, A.H., 1980. Frictional heating, fluid pressure, and the resistance to fault motion. J. Geophys. Res. Solid Earth 85, 6097–6112.
Langhans, M.H., Jaumann, R., Stephan, K., Brown, R., Buratti, B.J., Clark, R.N., Baines, K.H., Nicholson, P.D., Lorenz, R.D., Soderblom, L.A., Soderblom, J.M., Sotin, C., Barnes, J.W., Nelson, R., 2012. Titan's fluvial valleys: morphology, distribution, and spectral properties. Planet. Space Sci. 60, 34–51. https://doi.org/10.1016/j.pss.2011.01.020.
Lavvas, P.P., Coustenis, A., Vardavas, I.M., 2008. Coupling photochemistry with haze formation in Titan's atmosphere, Part II: results and validation with Cassini/Huygens data. Planet. Space Sci. 56, 67–99. https://doi.org/10.1016/j.pss.2007.05.027.
Le Corre, L., Le Mouélic, S., Sotin, C., Combe, J.P., Rodriguez, S., Barnes, J.W., Brown, R.H., Buratti, B.J., Jaumann, R., Soderblom, J., Soderblom, L.A., 2009. Analysis of a cryolava flow-like feature on Titan. Planet. Space Sci. 57, 870–879.
Le Gall, A., Janssen, M.A., Paillou, P., Lorenz, R.D., Wall, S.D., 2010. Radar-bright channels on Titan. Icarus 207, 948–958.
Le Gall, A., Janssen, M.A., Wye, L.C., Hayes, A.G., Radebaugh, J., Savage, C., Zebker, H., Lorenz, R.D., Lunine, J.I., Kirk, R.L., Lopes, R.M.C., 2011. Cassini SAR, radiometry, scatterometry and altimetry observations of Titan's dune fields. Icarus 213, 608–624.
Le Gall, A., Hayes, A.G., Ewing, R., Janssen, M.A., Radebaugh, J., Savage, C., Encrenaz, P., 2012. Latitudinal and altitudinal controls of Titan's dune field morphometry. Icarus 217, 231–242.
Le Mouélic, S., Cornet, T., Rodriguez, S., Sotin, C., Seignovert, B., Barnes, J.W., Brown, R.H., Baines, K.H., Buratti, B.J., Clark, R.N., Nicholson, P.D., 2019. The Cassini VIMS archive of Titan: from browse products to global infrared color maps. Icarus 319, 121–132.
Leier, A.L., DeCelles, P.G., Pelletier, J.D., 2005. Mountains, monsoons, and megafans. Geology 33, 289–292.
Liu, Z.Y., Radebaugh, J., Harris, R.A., Christiansen, E.H., Neish, C.D., Kirk, R.L., Lorenz, R.D., the Cassini RADAR team, 2016a. The tectonics of Titan: global structural mapping from Cassini RADAR. Icarus 270, 14–29.
Liu, Z.Y.C., Radebaugh, J., Harris, R.A., Christiansen, E.H., Rupper, S., 2016b. Role of fluids in the tectonic evolution of Titan. Icarus 270, 2–13.
Lopes, R.M., Mitchell, K.L., Stofan, E.R., Lunine, J.I., Lorenz, R., Paganelli, F., Kirk, R.L., Wood, C.A., Wall, S.D., Robshaw, L.E., Fortes, A.D., 2007. Cryovolcanic features on Titan's surface as revealed by the Cassini Titan Radar Mapper. Icarus 186, 395–412.
Lopes, R.M.C., Stofan, E.R., Pecyno, R., Radebaugh, J., Mitchell, K.L., Mitri, G., Wood, C.A., Kirk, R.L., Wall, S.D., Lunine, J.L., Hayes, A., Lorenz, R., Farr, T., Wye, L., Craig, J., Ollerenshaw, R., Janssen, M., LeGall, A., Paganelli, F., West, R., Stiles, B., Callahan, P., Anderson, Y., Valora, P., Soderblom, L., the Cassini RADAR Team, 2010. Distribution and interplay of geologic processes on Titan from Cassini radar data. Icarus 205, 540–558. https://doi.org/10.1016/j.icarus.2009.08.010.
Lopes, R.M.C., Kirk, R.L., Mitchell, K.L., Le Gall, A., Barnes, J.W., Hayes, A., Kargel, J., Wye, L., Radebaugh, J., Stofan, E.R., Janssen, M., Neish, C., Wall, S., Wood, C.A., Lunine, J.I., Malaska, M.J., 2013. Cryovolcanism on Titan: new results from Cassini RADAR and VIMS. J. Geophys. Res. Planet 118, 1–20. https://doi.org/10.1002/jgre.20062.
Lopes, R.M.C., Malaska, M.J., Solomonidou, A., Le Gall, A., Janssen, M.A., Neish, C.D., Turtle, E.P., Birch, S.P.D., Hayes, A.G., Radebaugh, J., Coustenis, A., Schoenfeld, A., Stiles, B.W., Kirk, R.L., Mitchell, K.L., Stofan, E.R., Lawrence, K.J., the Cassini RADAR Team, 2016. Nature, distribution, and origin of Titan's undifferentiated plains. Icarus 270, 162–182. https://doi.org/10.1016/j.icarus.2015.11.034.
Lopes, R.M., Malaska, M., Schoenfeld, A., Solomonidou, A., Williams, D.D., Birch, S., Le Gall, A.A., Radebaugh, J., 2019. Geomorphological map of the Soi crater region on Titan. In: AGU Fall Meeting 2019. AGU. December.
Lopes, R.M.L., Malaska, M.J., Schoenfeld, A.M., Solomonidou, A., Birch, S.P.D., Florence, M., Hayes, A.G., Williams, D.A., Radebaugh, J., Verlander, T., Turtle, E.P., Le Gall, A., Wall, S., the Cassini RADAR Team, 2020. A global geomorphological map of Saturn's Moon Titan. Nat. Astr. 4, 228–233.
Lora, J.M., Lunine, J.I., Russell, J.L., 2014. GCM Simulations of Titan's Middle and Lower Atmosphere and Comparison to Observations. Available from: <arXiv: 1412.7995> [astro-ph.EP].
Lorenz, R.D., 1993. The life, death and afterlife of a raindrop on Titan. Planet. Space Sci. 41, 647–655.
Lorenz, R.D., 2000. The weather on Titan. Science 290, 467–468.
Lorenz, R.D., Lunine, J.I., 1996. Erosion on Titan: past and present. Icarus 196, 79–91.
Lorenz, R.D., Wall, S., Radebaugh, J., Boubin, G., Reffet, E., Janssen, M., Stofan, E., Lopes, R., Kirk, R., Elachi, C., Lunine, J., Mitchell, K., Paganelli, F., Soderblom, L., Wood, C., Wye, L., Zebker, H., Anderson, Y., Ostro, S., Allison, M., Boehmer, R., Callahan, P., Encrenaz, P., Ori, G.G., Francescitti, G., Gim, Y., Hamilton, G., Hensley, S., Johnson, W., Kelleher, K., Muhleman, D., Picardi, G., Posa, F., Roth, L., Seu, R., Shaffer, S., Stiles, B., Vetrella, S., Flamini, E., West, R., 2006. The Sand Seas of Titan: Cassini RADAR observations of longitudinal dunes. Science 312, 724–727. https://doi.org/10.1126/science.1123257.
Lorenz, R.D., Wood, C.A., Lunine, J.I., Wall, S.D., Lopes, R.M., Mitchell, K.L., Paganelli, F., Anderson, Y.Z., Wye, L., Tsai, C., Zebker, H., Stofan, E.R., 2007. Titan's young surface: initial impact crater survey by Cassini RADAR and model comparison. Geophys. Res. Lett. 34, L07204 https://doi.org/10.1029/2006GL028971.
Lorenz, R.D., Lopes, R.M., Paganelli, F., Lunine, J.I., Kirk, R.L., Mitchell, K.L., Soderblom, L.A., Stofan, E.R., Ori, G., Myers, M., Miyamoto, H., 2008. Fluvial channels on Titan: initial Cassini RADAR observations. Planet. Space Sci. 56, 1132–1144.
Lorenz, R.D., Stiles, B.W., Aharonson, O., Lucas, A., Hayes, A.G., Kirk, R.L., Zebker, H.A., Turtle, E.P., Neish, C.D., Stofan, E.R., Barnes, J.W., the Cassini RADAR Team, 2013.

A global topographic map of Titan. Icarus 225, 367–377. https://doi.org/10.1016/j.icarus.2013.04.002.
Lucas, A., Rodriguez, S., Narteau, C., Charnay, B., Du Pont, S.C., Tokano, T., Garcia, A., Thiriet, M., Hayes, A.G., Lorenz, R.D., Aharonson, O., 2014. Growth mechanisms and dune orientation on Titan. Geophys. Res. Lett. 41 (17), 6093–6100.
Lunine, J.I., Atreya, S.K., 2008. The methane cycle on Titan. Nat. Geosci. 1, 159–164.
Lunine, J.I., Lorenz, R.D., 2009. Rivers, lakes, dunes, and rain: crustal processes in Titan's methane cycle. Annu. Rev. Earth Planet. Sci. 37, 299–320.
Lunine, J.I., Stevenson, D.J., 1987. Clathrate and ammonia hydrates at high pressure: application to the origin of methane on Titan. Icarus 70, 61–77.
Lunine, J., Artemieva, N., Lorenz, R., Flamini, E., 2005. Numerical modeling of impact cratering on Titan with implications for the age of Titan's surface. Lunar Planet. Sci. 36. Abstract 1504.
Lunine, J.I., Elachi, C., Wall, S.D., Janssen, M., Allison, M.D., Anderson, Y., Boehmer, R., Callahan, P., Encrenaz, P., Flamini, E., Franceschetti, G., Gim, Y., Hamilton, G., Hensley, S., Johnson, W.T.K., Kelleher, K., Kirk, R.L., Lopes, R.M., Lorenz, R., Muhlemen, D.O., Orosei, R., Ostro, S.J., Paganelli, F., Paillou, P., Picardi, G., Posa, F., Radebaugh, J., Roth, L.E., Seu, R., Shaffer, S., Soderblom, L.A., Stiles, B., Stofan, E.R., Vetrella, S., West, R., Wood, C.A., Wye, L., Zebker, H., Alberti, G., Karkoschka, E., Rizk, B., McFarlane, E., See, C., Kazeminejad, B., 2008. Titan's diverse lanscapes as evidenced by Cassini RADAR's third and fourth looks at Titan. Icarus 195, 415–433. https://doi.org/10.1016/j.icarus.2007.12.022.
MacKenzie, S.M., Barnes, J.W., Sotin, C., Soderblom, J.M., Le Mouélic, S., Rodriguez, S., Baines, K.H., Buratti, B.J., Clark, R.N., Nicholson, P.D., McCord, T.B., 2014. Evidence of Titan's climate history from evaporite distribution. Icarus 243, 191–207.
Malaska, M.J., Hodyss, R., 2014. Dissolution of benzene, naphthalene, and biphenyl in a simulated Titan lake. Icarus 242, 74–81. https://doi.org/10.1016/j.icarus.2014.07.022.
Malaska, M., Radebaugh, J., Lorenz, R., Mitchell, K., Farr, T., Stofan, E., 2010. Identification of Karst-like Terrain on Titan from Valley Analysis. Lunar and Planetary Science Conference XLI, Abstract #1544.
Malaska, M., Radebaugh, J., Mitchell, K., Lopes, R., Wall, S., Lorenz, R., 2011. Surface dissolution model for Titan karst. In: Oral presentation at the First International Planetary Cave Research Workshop, Carlsbad, NM, October 2011. Abstract 8018.
Malaska, M.J., Lopes, R.M.C., Williams, D.A., Neish, C.D., Solomonidou, A., Soderblom, J. M., Schoenfeld, A.M., Birch, S.P.D., Hayes, A.G., Le Gall, A., Janssen, M.A., Farr, T. G., Lorenz, R.D., Radebaugh, J., Turtle, E.P., 2016a. Geomorphological map of the Afekan Crater region, Titan: terrain relationships in the equatorial and mid-latitude regions. Icarus 270, 130–161. https://doi.org/10.1016/j.icarus.2016.02.021.
Malaska, M.J., Lopes, R.M., Hayes, A.G., Radebaugh, J., Lorenz, R.D., Turtle, E.P., 2016b. Material transport map of Titan: the fate of dunes. Icarus 270, 183–196. https://doi.org/10.1016/j.icarus.2015.09.029.
Malaska, M.J., Radebaugh, J., Lopes, R.M., Mitchell, K.L., Verlander, T., Schoenfeld, A. M., Florence, M.M., Le Gall, A., Solomonidou, A., Hayes, A.G., Birch, S.P., 2020. Labyrinth terrain on Titan. Icarus 113764.
Malin, M.C., Caplinger, M.A., Davis, S.D., 2001. Observational evidence for an active surface reservoir of solid carbon dioxide on Mars. Science 294, 2146–2148.
Martin, E.S., Kattenhorn, S.A., Collins, G.C., Michaud, R.L., Pappalardo, R.T., Wyrick, D. Y., 2017. Pit chains on Enceladus signal the recent tectonic dissection of the ancient cratered terrains. Icarus 294, 209–217.
McKenzie, D., Brune, J.N., 1972. Melting on fault planes during large earthquakes. Geophys. J. Int. 29, 65–78.
Mitchell, K.L., Malaska, M., 2011. Karst on Titan, First International Planetary Cave Research Workshop, October 2011, Carlsbad, New Mexico, Abstract #8021.
Mitri, G., Showman, A.P., Lunine, J.I., Lorenz, R.D., 2007. Hydrocarbon lakes on Titan. Icarus 186, 385–394.
Mitri, G., Bland, M.T., Showman, A.P., Radebaugh, J., Stiles, B., Lopes, R.M.C., Lunine, J. I., Pappalardo, R.T., 2010. Mountains on Titan: modeling and observations. J. Geophys. Res. Planet 115, E10002. https://doi.org/10.1029/2010/JE003592.
Mitri, G., Lunine, J.I., Mastrogiuseppe, M., Poggiali, V., 2019. Possible explosion crater origin of small lake basins with raised rims on Titan. Nat. Geosci. 12, 791–796.
Moore, J.M., Pappalardo, R.T., 2011. Titan: an exogenic world? Icarus 212, 790–806.
Mousis, O., Guilbert-Lepoutre, A., Brugger, B., Jorda, L., Kargel, J.S., Bouquet, A., Auger, A.T., Lamy, P., Vernazza, P., Thomas, N., Sierks, H., 2015. Pits formation from volatile outgassing on 67P/Churyumov–Gerasimenko. Astrophys. J. Lett. 814, L5.
Neish, C.D., Lorenz, R.D., 2012. Titan's global crater population: a new assessment. Planet. Space Sci. 60, 26–33. https://doi.org/10.1016/j.psss.2011.02.016.
Neish, C.D., Lorenz, R.D., Kirk, R.L., Wye, L.C., 2010. Radarclinometry of the sand seas of Africa's Namibia and Saturn's moon Titan. Icarus 208, 385–394.
Neish, C.D., Kirk, R.L., Lorenz, R.D., Bray, V.J., Schenk, P., Stiles, B.W., Turtle, E., Mitchell, K., Hayes, A., Cassini RADAR Team, 2013. Crater topography on Titan: Implications for landscape evolution. Icarus 223, 82–90.
Neish, C.D., Barnes, J.W., Sotin, C., MacKenzie, S., Soderblom, J.M., Le Mouélic, S., Kirk, R.L., Stiles, B.W., Malaska, M.J., Le Gall, A., Brown, R.H., Baines, K.H., Buratti, B., Clark, R.N., Nicholson, P.D., 2015. Spectral properties of Titan's impact craters imply chemical weathering of its surface. Geophys. Res. Lett. 42, 3746–3754. https://doi.org/10.1002/2015GL063824.
Nelson, R.M., Kamp, L.W., Lopes, R.M.C., Matson, D.L., Kirk, R.L., Hapke, B.W., Wall, S. D., Boryta, M.D., Leader, F.E., Smythe, W.D., Mitchell, K.L., Baines, K.H., Jaumann, R., Sotin, C., Clark, R.N., Cruikshank, D.P., Drossart, P., Lunine, J.I., Combes, M., Bellucci, G., Bibring, J.-P., Capaccioni, F., Cerroni, P., Coradini, A., Formisano, V., Filacchione, G., Langevin, Y., McCord, T.B., Mennella, V., Nicholson, P.D., Sicardy, B., Irwin, P.G.J., 2009. Photometric changes on Saturn's Moon Titan: evidence for cryovolcanism. Geophys. Res. Lett. 36, L04202 https://doi.org/10.1029/2008GL036206.
Newton, J.G., 1987. Development of Sinkholes Resulting from Man's Activities in the Eastern United States (No. 968–969). US Geological Survey.
Newton, J.G., Hyde, L.W., 1971. Sinkhole Problem in and Near Roberts Industrial Subdivision, Birmingham, Alabama. Alabama Geological Survey Circ, 68, p. 49.
Paganelli, F., Janssen, M.A., Lopes, R.M., Stofan, E., Wall, S.D., Lorenz, R.D., Lunine, J.I., Kirk, R.L., Roth, L., Elachi, C., Team, T.C.R., 2008. Titan's surface from the Cassini RADAR radiometry data during SAR mode. Planet. Space Sci. 56, 100–108.
Pappalardo, R.T., Collins, G.C., 2005. Strained craters on ganymede. J. Struct. Geol. 27, 827–838.
Perron, J.T., Lamb, M.P., Koven, C.D., Fung, I.Y., Yager, E., Ádámkovics, M., 2006. Valley formation and methane precipitation rates on Titan. J. Geophys. Res. 111, E11001 https://doi.org/10.1029/2005JE002602.
Porco, C.C., West, R.A., Squyres, S., McEwen, A., Thomas, P., Murray, C.D., Delgenio, A., Ingersoll, A.P., Johnson, T.V., Neukum, G., Veverka, J., Dones, L., Brahic, A., Burns, J.A., Haemmerle, V., Knowles, B., Dawson, D., Roatsch, T., Beurle, K., Owen, W., 2004. Cassini imaging science: instrument characteristics and anticipated scientific investigations at Saturn. Space Sci. Rev. 115, 363–497. https://doi.org/10.1007/s11214-004-1456-7.
Radebaugh, J., Lorenz, R.D., Kirk, R.L., Lunine, J.I., Stofan, E.R., Lopes, R.M.C., Wall, S. D., 2007. Mountains on Titan as observed by Cassini Radar. Icarus 192, 77–91. https://doi.org/10.1016/j.icarus.2007.026.020.
Radebaugh, J., Lorenz, R.D., Lunine, J.I., Wall, S.D., Boubin, G., Reffet, E., Kirk, R.L., Lopes, R.M., Stofan, E.R., Soderblom, L., Allison, M., Janssen, M., Paillouo, P., Callahan, P., Spencer, C., Cassini RADAR Team, 2008. Dunes on Titan observed by Cassini Radar. Icarus 194, 690–703. https://doi.org/10.1016/j.icarus.2007.10.015.
Radebaugh, J., Lorenz, R., Farr, T., Paillou, P., Savage, C., Spencer, C., 2010. Linear dunes on Titan and earth: initial remote sensing comparisons. Geomorphology 121, 122–132. https://doi.org/10.1016/j.geomorph.2009.09.02.022.
Radebaugh, J., Ventra, D., Lorenz, R.D., Farr, T., Kirk, R., Hayes, A., Malaska, M.J., Birch, S., Liu, Z.Y.C., Lunine, J., Barnes, J., 2018. Alluvial and fluvial fans on Saturn's moon Titan reveal processes, materials and regional geology. Geol. Soc. Lond., Spec. Publ. 440, 281–305.
Schaber, G.G., Berlin, G.L., Brown Jr., W.E., 1976. Variations in surface roughness within Death Valley, California: geologic evaluation of 25-cm-wavelength radar images. Geol. Soc. Am. Bull. 87, 29–41.
Scholz, C.H., 1980. Shear heating and the state of stress on faults. J. Geophys. Res. Solid Earth 85, 6174–6184.
Seignovert, B., Le Mouélic, S., Brown, R.H., Joseph, E., Karkoschka, E., Pasek, V., Sotin, C., Turtle, E.P., 2019. Titan's Global Map Combining VIMS and ISS Mosaics. EPSC, 2019, EPSC-DPS2019.
Sinclair, W.C., 1982. Sinkhole Development Resulting from Ground-Water Withdrawal in the Tampa Area, Florida (81–50). US Geological Survey, Water Resources Division.
Soderblom, L.A., Kirk, R.L., Lunine, J.I., Anderson, J.A., Baines, K.H., Barnes, J.W., Barrett, J.M., Brown, R.H., Buratti, B.J., Clark, R.N., Cruikshank, D.P., Elachi, C., Janssen, M.A., Jaumann, R., Karkoschka, E., Le Mouélic, S., Lopes, R.M., Lorenz, R. D., McCord, T.B., Nicholson, P.D., Radebaugh, J., Rizk, B., Sotin, C., Stofan, E.R., Sucharski, T.L., Tomasko, M.G., Wall, S.D., 2007. Correlations between Cassini VIMS spectra and RADAR SAR images: implications for Titan's surface composition and the character of the Huygens Probe Landing Site. Planet. Space Sci. 55, 2025–2036. https://doi.org/10.1016/j.pss.2007.04.014.
Solomonidou, A., Hirtzig, M., Coustenis, A., Bratisolis, E., le Mouelic, S., Rodriguez, S., Stephan, K., Drossart, P., Sotin, C., Jaumann, R., Bornw, R.H., Kyriakopoulos, K., Lopes, R.M.C., Bampasidis, G., Stamatelopoulou-Seymour, K., Moussas, X., 2014. Surface albedo properties of geologicaly interesting areas on Titan. J. Geophys. Res. 119, 1729–1747. https://doi.org/10.1002/2014JE004634.
Solomonidou, A., Coustenis, A., Lopes, R.M., Malaska, M.J., Rodriguez, S., Drossart, P., Elachi, C., Schmitt, B., Philippe, S., Janssen, M., Hirtzig, M., 2018. The spectral nature of Titan's major geomorphological units: constraints on surface composition. J. Geophys. Res. Planet 123, 489–507.
Solomonidou, A., Neish, C., Coustenis, A., Malaska, M., Le Gall, A., Lopes, R., Werynski, A., Lawrence, K., Altobelli, N., Witasse, O., Schoenfeld, A., Matsoukas, C., Baziotis, I., Drossart, P., 2020a. The chemical composition of impact craters on Titan: implications for exogenic processing. Astron. Astrophys. 641 (A16), 1–14.
Solomonidou, A., Le Gall, A., Malaska, M.J., Birch, S.P.D., Lopes, R.M.C., Coustenis, A., Rodriguez, S., Wall, S.D., Michaelides, R.J., Nasr, M.R., Elachi, C., 2020b. Spectral and emissivity analysis of the raised ramparts around Titan's northern lakes. Icarus 344, 113338.
Sotin, C., Jaumann, R., Buratti, B.J., Brown, R.H., Clark, R.N., Soderblom, L.A., Baines, K. H., Bellucci, G., Bibring, J.P., Capaccioni, F., Cerroni, P., 2005. Release of volatiles from a possible cryovolcano from near-infrared imaging of Titan. Nature 435, 786–789.
Spigner, B.C., 1978. Review of Sinkhole-collapse Problems in a Carbonate Terrane (The Commission).
Stiles, B.W., Hensley, S., Gim, Y., Bates, D.M., Kirk, R.L., Hayes, A., Radebaugh, J., Lorenz, R.D., Mitchell, K.L., Callahan, P.S., Zebker, H., Johnson, W.T.K., Wall, S.D., Wood, C.A., Janssen, M., Pelletier, F., West, R.D., Veramacheneni, C., Cassini RADAR Team, 2009. Determining Titan surface topography from Cassini SAR data. Icarus 202, 584–598. https://doi.org/10.1016/j.icarus.2009.03.032.
Stock, J.D., 2013. 9.23 Waters Divided: A History of Alluvial Fan Research and a View of Its Future.
Stofan, E.R., Elachi, C., Lunine, J.I., Lorenz, R.D., Stiles, B., Mitchell, K.L., Ostro, S., Soderblom, L., Wood, C., Zebker, H., Wall, S., Janssen, M., Kirk, R., Lopes, R., Paganelli, F., Radebaugh, J., Wye, L., Anderson, Y., Allison, M., Boehmer, R., Callahan, P., Encrenaz, P., Flamini, E., Francescetti, G., Gim, Y., Hamilton, G., Hensley, S., Johnson, W.T.K., Kelleher, K., Muhlman, D., Paillou, P., Picardi, G.,

Posa, F., Roth, Seu R., Shaffer, S., Vetrella, S., West, R., 2007. The lakes of Titan. Nature 445, 61–64. https://doi.org/10.1038/nature05438.
Tanaka, K.L., Golombek, M.P., 1989. Martian tension fractures and the formation of grabens and collapse features at Valles Marineris. In: Lunar and Planetary Science Conference Proceedings, vol. 19, pp. 383–396.
Telfer, M.W., Radebaugh, J., Cornford, B., Lewis, C., 2019. Long-wavelength sinuosity of linear dunes on Earth and Titan and the effect of underlying topography. J. Geophys. Res. Planet 124, 2369–2381.
Thelen, A.E., Nixon, C.A., Chanover, N.J., Cordiner, M.A., Molter, E.M., Teanby, N.A., Irwin, P.G.J., Serigano, J., Charnley, S.B., 2019. Abundance measurements of Titan's stratospheric HCN, HC3N, C3H4, and CH3CN from ALMA observations. Icarus 319, 417–432.
Thomas, P.C., Malin, M.C., Edgett, K.S., Carr, M.H., Hartmann, W.K., Ingersoll, A.P., James, P.B., Soderblom, L.A., Veverka, J., Sullivan, R., 2000. North–south geological differences between the residual polar caps on Mars. Nature 404, 161–164.
Tomasko, M.G., Archinal, B., Becker, T., Bézard, B., Bushroe, M., Combes, M., Cook, D., Coustenis, A., De Bergh, C., Dafoe, L.E., Doose, L., 2005. Rain, winds and haze during the Huygens probe's descent to Titan's surface. Nature 438, 765–778.
Turtle, E.P., Perry, J.E., Hayes, A.G., Lorenz, R.D., Barnes, J.W., McEwen, A.S., West, R. A., Del Genio, A.D., Barbara, J.M., Lunine, J.I., Schaller, E.L., Ray, T.L., Lopes, R.M. C., Stofan, E.R., 2011. Rapid and extensive surface changes near Titan's equator: evidence of April showers. Science 331, 1414–1417. https://doi.org/10.1126/science.1201063.
Vincent, J.B., Bodewits, D., Besse, S., Sierks, H., Barbieri, C., Lamy, P., Rodrigo, R., Koschny, D., Rickman, H., Keller, H.U., Agarwal, J., 2015. Large heterogeneities in comet 67P as revealed by active pits from sinkhole collapse. Nature 523, 63–66.
Wall, S.D., Lopes, R.M., Stofan, E.R., Wood, C.A., Radebaugh, J.L., Hörst, S.M., Stiles, B. W., Nelson, R.M., Kamp, L.W., Janssen, M.A., Lorenz, R.D., 2009. Cassini RADAR images at Hotei Arcus and western Xanadu, Titan: evidence for geologically recent cryovolcanic activity. Geophys. Res. Lett. 36.
Waltham, A.C., Bell, F.G., Culshaw, M.G., 2005. Sinkholes and Subsidence: Karst and Cavernous Rocks in Engineering and Construction. Springer Science & Business Media.
Werynski, A., Neish, C.D., Le Gall, A., Janssen, M.A., Cassini RADAR Team, 2019. Compositional variations of Titan's impact craters indicates active surface erosion. Icarus 321, 508–521.
Williams, D.A., Radebaugh, J., Lopes, R.M.C., Stofan, E., 2011. Geomorphologic mapping of the Menrva region of Titan using *Cassini* RADAR data. Icarus 212, 744–750. https://doi.org/10.1016/j.icarus.2011.01.014.
Wilson, I.G., 1971. Desert sand flow basins and a model for the development of ergs. Geogr. J. 180–199.
Wilson, E.H., Atreya, S.K., 2004. Current state of modeling the photochemistry of Titan's mutually dependent atmosphere and ionosphere. J. Geophys. Res. 109 https://doi.org/10.1029/2003JE002181. E06002.
Wood, C.A., Radebaugh, J., 2020. Morphologic evidence for volcanic Craters near Titan's North Polar Region May 28, 2020. J. Geophys. Res. Planet 125 (8), 1–16 e2019JE006036.
Wood, C.A., Lorenz, R., Kirk, R., Lopes, R., Mitchell, K., Stofan, E., the Cassini RADAR Team, 2010. Impact craters on Titan. Icarus 206 (2010), 334–344. https://doi.org/10.1016/j.icarus.2009.08.021.
Wye, L.C., Zebker, H.A., Ostro, S.J., West, R.D., Gim, Y., Lorenz, R.D., Cassini RADAR Team, 2007. Electrical properties of Titan's surface from Cassini RADAR scatterometer measurements. Icarus 188 (2), 367–385.
Wyrick, D., Ferrill, D.A., Morris, A.P., Colton, S.L., Sims, D.W., 2004. Distribution, morphology, and origins of Martian pit crater chains. J. Geophys. Res. Planet 109.